

# POLAMI: Polarimetric Monitoring of Active Galactic Nuclei at Millimetre Wavelengths

## III. Characterisation of total flux density and polarisation variability of relativistic jets

Iván Agudo<sup>1★</sup>, Clemens Thum<sup>2†</sup>, Venkatesh Ramakrishnan<sup>3,4</sup>, Sol N. Molina<sup>1</sup>, Carolina Casadio<sup>5,1</sup> and José L. Gómez<sup>1</sup>

<sup>1</sup>*Instituto de Astrofísica de Andalucía (CSIC), Apartado 3004, E-18080 Granada, Spain*

<sup>2</sup>*Instituto de Radio Astronomía Millimétrica, Avenida Divina Pastora, 7, Local 20, E-18012 Granada, Spain*

<sup>3</sup>*Aalto University Metsähovi Radio Observatory, Metsähovintie 114, 02540, Kylmälä, Finland*

<sup>4</sup>*Universidad de Concepción, Departamento de Astronomía, Casilla 160-C, Concepción, Chile*

<sup>5</sup>*Max-Planck-Institut für Radioastronomie, Auf dem Hügel, 69, D-53121, Bonn, Germany*

Accepted XXX. Received YYY; in original form ZZZ

### ABSTRACT

We report on the first results of the POLAMI program, a simultaneous 3.5 and 1.3 mm full-Stokes-polarisation monitoring of a sample of 36 of the brightest active galactic nuclei in the northern sky with the IRAM 30m Telescope. Through a systematic statistical study of data taken from October 2006 (from December 2009 for the case of the 1.3 mm observations) to August 2014, we characterise the variability of the total flux density and linear polarisation. We find that all sources in the sample are highly variable in total flux density at both 3.5 and 1.3 mm, as well as in spectral index, that (except in particularly prominent flares) is found to be optically thin between these two wavelengths. The total flux-density variability at 1.3 mm is found, in general, to be faster, and to have larger fractional amplitude and flatter power-spectral-density slopes than 3.5 mm. The polarisation degree is on average larger at 1.3 mm than at 3.5 mm, by a factor of 2.6. The variability of linear polarisation degree is faster and has higher fractional amplitude than for total flux density, with the typical time scales during prominent polarisation peaks being significantly faster at 1.3 mm than at 3.5 mm. The polarisation angle at both 3.5 and 1.3 mm is highly variable. Most of the sources show one or two excursions of  $> 180^\circ$  on time scales from a few weeks to about a year during the course of our observations. The 3.5 and 1.3 mm polarisation angle evolution follow rather well each other, although the 1.3 mm data show a clear preference to more prominent variability on the short time scales, i.e. weeks. The data are compatible with multi-zone models of conical jets involving smaller emission regions for the shortest-wavelength emitting sites. Such smaller emitting regions should also be more efficient in energising particle populations, as implied by the coherent evolution of the spectral index and the total flux density during flaring activity of strong enough sources. The data also favours the integrated emission at 1.3 mm to have better ordered magnetic fields than the one at 3.5 mm.

**Key words:** Galaxies: active – galaxies: jets – quasars: general – BL Lacertae objects: general – polarisation – surveys

### 1 INTRODUCTION

Radio-loud active galactic nuclei (AGN) are among the most powerful emitters at spectral ranges from radio to  $\gamma$ -rays. Rapid and strong variability is one of the most salient properties of radio-loud AGN, which is inherent to the relativis-

★ E-mail: iagudo@iaa.es (IA)

† E-mail: thum@iram.es (CT)

tic nature of their powerful jets (e.g. Marscher et al. 2008; Abdo et al. 2010; Aleksić et al. 2015). The millimetre-range jet emission is produced by the synchrotron process in the presence of magnetic fields (that are also an essential ingredient for the jet-formation mechanism, e.g. Tchekhovskoy 2015), which makes the emission significantly polarised (e.g. Marscher et al. 2010; Agudo et al. 2011b).

Recent polarisation variability studies of AGN have demonstrated to be a powerful tool to deepen our understanding of the relativistic jet phenomenon. Polarisation observations carry information about the magnetic fields responsible for the AGN jet emission, and allow us to constrain the possible physical conditions of the emitting plasma by eliminating some degrees of freedom inherent to non-polarimetric observations. They also allow us to identify individual events (and even emission regions) along the spectrum by comparing similar polarimetric properties and time-dependent behaviour (e.g. Marscher et al. 2010; Abdo et al. 2010). In particular, short millimetre observations have proven to be instrumental in these tasks (specially when combined with multi-spectral-range monitoring) when well-sampled time-evolution tracks of the polarimetric properties of radio loud AGN are compiled (e.g. Jorstad et al. 2010, 2013; Agudo et al. 2011a,b). This is mainly because short mm wavelengths access the innermost regions of relativistic jets where their synchrotron emission is optically thin (Jorstad et al. 2007; Agudo et al. 2014). At millimetre wavelengths, typical Faraday rotation measures are in the range of  $10^2$  to  $10^5$  rad m $^{-2}$  (e.g., Zavala & Taylor 2004) implying that the associated small Faraday depths only mildly modify the intrinsic polarisation angles.

In the current study (the third of a series of three, Paper III hereafter), we focus on the properties of the total flux density (total flux hereafter) and linear polarisation variability for a sample of 36 of the brightest radio-loud AGN monitored within the POLAMI program (Polarimetric Monitoring of AGN with Millimetre Wavelengths, see <http://polami.iaa.es>) at 3.5 mm and 1.3 mm<sup>1</sup> with the IRAM 30m Telescope. The 3 mm observations presented here were performed from October 2006 to August 2014, with a median sampling of 22 days, and slightly faster, 19 days, after 2010. The simultaneous 1 mm observations were performed from December 2009 only, therefore not covering the first three years of 3 mm observations. Despite this partial mismatch, we also study in this work the interrelation of the variability at the two observing bands. This paper complements the POLAMI results that are presented in Agudo et al. (2017, Paper I hereafter) where we provide the basic information regarding this long-term monitoring program (including sample selection, observing strategy, and data reduction and calibration), and Thum et al. (2017, Paper II hereafter) where we focus on the circular polarisation properties of the sample. Further publications on the results of the comparison of the POLAMI data with the  $\gamma$ -ray, optical polarimetric, and 7 mm VLBI polarimetric behaviour of the sample of sources is already in preparation, together with more detailed studies of particularly interesting sources or events.

<sup>1</sup> For easier reading, hereafter we will use 3 mm and 1 mm instead of 3.5 mm and 1.3 mm, respectively.

Here, in Paper III we present our results regarding long-term variability of the sample of targets (Section 2), and we discuss the implication of those observing results (Section 3), first in terms of total flux (Section 3.1), and then in linear polarisation degree (Section 3.3), and linear polarisation angle (Section 3.5). The inter-relation of the total flux variability with the linear polarisation is discussed in Section 3.8, whereas the summary and main conclusions of our work are presented in Section 4.

## 2 RESULTS

The end product of our observations, that were acquired and calibrated as discussed in detail in Paper I, is presented in Fig. 11. This figure shows the time evolution of the daily averages of the 3 and 1 mm fully calibrated measurements of total flux ( $S$ ), linear polarisation degree ( $m_L$ ), and linear polarisation angle ( $\chi$ ), for the 36 variable sources in the POLAMI sample<sup>2</sup> Figure 11 also includes the comparison of  $S$ ,  $m_L$ , and  $\chi$  at the two observing wavelengths, by providing measurements of spectral index ( $\alpha$ ), ratio of 1 mm to 3 mm linear polarisation degree ( $m_{L,1}/m_{L,3}$ ), and rotation measure (RM).

For defining the 3 mm polarisation angle ( $\chi_3$ ) curves, we took care of the  $n\pi$ -ambiguity of the polarisation vector. Although we tested several different methods (mainly following the prescriptions by Kiehlmann et al. 2016), we found that there is no optimum method for all modes of  $\chi_3$  variability and uneven time sampling on our data set. We therefore chose the simplest method among all tested ones that still gave point-to-point smooth variations of the polarisation angle. For this, we adopted a procedure for rotation of  $\chi_3$  measurements such that every third point was rotated by  $\pm n \times \pi$  if the angle difference with the weighted mean of the two preceding points was larger than  $\pi/2$ , with  $n$  being a natural number selected to minimise such angle difference. For the 1 mm polarisation angle measurements ( $\chi_1$ ), we applied rotations by  $\pm m \times \pi$  so that  $|\chi_3 - \chi_1| < \pi/2$  for the final representation of every independent  $\chi_1$  measurements and its corresponding  $\chi_3$ .

## 3 DISCUSSION

The methods and definitions employed for the characterisation and the analysis of the total flux and polarisation variability are described in Appendix A. These include a standard  $\chi^2$  test for variability, a power spectral density (PSD) analysis for the estimation of the PSD slopes, a definition of the fractional variability amplitude ( $F$ ), and a method for computing the discrete correlation function based on a Monte Carlo simulation scheme for the assessment of the statistical significance of correlations peaks. The following subsections describe the results obtained from implementing these analysis tools and definitions on the data sets, as well as their astrophysical implications.

<sup>2</sup> Note that 1328+307 (3C 286) is a standard total flux and linear polarisation calibrator (see Agudo et al. 2012, and references therein) and has therefore not been included in this variability study.

### 3.1 Total flux variability

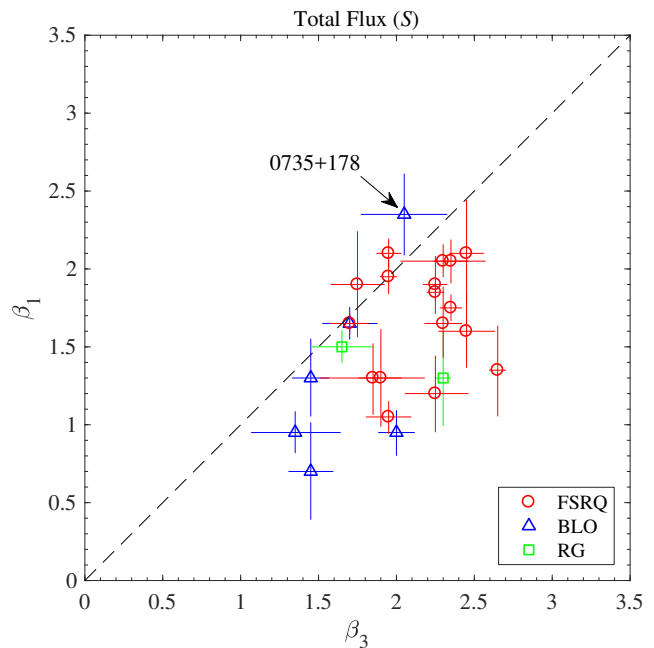
Figure 11 shows that all sources in the sample are strongly variable in total flux within the time range of our observations, both at 3 and 1 mm. Representative cases are 0829+046 and 1055+018, with maximum to minimum ratios of total flux by factors  $\sim 4$  at both wavelengths (see Table 1). These amplitudes are moderate compared to more extreme cases like 2251+158, with max/min ratio up to  $\approx 42$  at 1 mm ( $\approx 17$  at 3 mm), and 1406–076, with max/min  $\approx 2$  at both 3 and 1 mm.

Table 1 shows that all 36 sources show a probability to be variable of more than 99.73 % at both observing wavelengths. However, different variability modes are identified for different sources in the sample. This is clearly reflected in the formal variability analysis that we have performed for the total flux for every source in the sample (see Table 1 and subsections below).

The power spectral density (PSD) slope for 3 mm total flux ( $\beta_3$ ), computed for the time spanned between December 2009 and August 2014; i.e. the same one as the 1 mm data, shows a median  $\sim 1.9$  (Table 1). A small fraction of cases shows more prominent variability on the short time scales  $\lesssim 1$  month (with  $\beta_3 \lesssim 1.5$ ), e.g. 0716+714 and 2200+420. Others show a much smoother mode of variability on the short time scales, with  $\beta_3 \gtrsim 2.5$ , e.g. 0316+413, 0336–019, and 0836+710. The maximum and minimum of  $\beta_3$  are  $\sim 2.9$  for 0219+428 and  $\sim 0.6$  for 1219+285, respectively, but these extreme cases are affected by large uncertainties ( $\sim 2.9$ ) in the computation of  $\beta_3$ . The PSD slope at 1 mm ( $\beta_1$ ), with median  $\sim 1.6$ , shows, in general, significantly smaller PSD slopes (i.e. more prominent variability on the short time-scales with regard to the long ones) as for the total flux variability at 3 mm. This is clearly seen in Figure 1 which shows that the entire distribution of 3 mm PSD slopes is systematically shifted towards higher values as compared to those at 1 mm. Our results thus imply that, in general, radio-loud AGN show a tendency to display more prominent short time-scales of variability as compared to that at longer time-scales when observing wavelength decreases from 3 to 1 mm.

The 3 mm fractional variability amplitude ( $F_3$ , also shown in Table 1) reaches maximum and minimum levels of  $\sim 0.7$  (for 2251+158, a well known extremely variable source from 2008 to 2011), and  $\sim 0.1$  (for 1406–076 that did not show extreme fractional amplitude during our observations), respectively, but the typical (median)  $\tilde{F}_3 \sim 0.3$ , where the tilde denotes the median of  $F_3$ . The 1 mm fractional variability amplitude goes from  $\sim 0.9$  (for 0827+243 and 2251+158) to  $\sim 0.2$  (for the cases of 0316+413 and 1406–076), with typical (median)  $\tilde{F}_1 = 0.4$ . A comparison of  $F_3$ , computed by using the 3 mm flux densities in the same time span covered by the 1 mm data, and  $F_1$  also shows a general trend of  $F_1$  to display larger values than the corresponding  $F_3$  for a given source, see Fig. 2. Therefore the data demonstrate that, in general, the total flux variability of radio loud AGN at 1 mm have higher fractional amplitude than those at 3 mm.

To characterise the time scales of total flux variability for each one of the sources we use the zero-crossing time of the main lobe of the auto-correlation function (ACF), i.e.  $\tau_0$ , see Appendix A. Note that, by definition, the discrete correlation function (DCF, and therefore the ACF) are pri-



**Figure 1.** PSD slope ( $\beta$ , see Table 1) computed from the 1 mm total flux light curve of every source with regard to the corresponding one at 3 mm. Horizontal and vertical lines correspond to confidence intervals. The label FSRQ stands for flat spectrum radio quasars, where BLO and RG indicate BL Lac type objects and radio galaxies, respectively. Outliers of the distribution of points in this plot are labeled by their corresponding source name.

marily sensitive to the most prominent peaks in the data trains, and therefore  $\tau_0$  mainly provides a representation of the time scales of the most prominent outburst in the total-flux light curves. At 3 mm, the median of  $\tau_0$  for the entire sample is 318 days. However, time scales of prominent variability as large as 805 days (for 0735+178), and as small as 45 days (for 1101+384), are found in the data set. The time scale of total flux variability computed from  $\tau_0$  is also smaller at 1 mm (with a median of 197 days) as compared to that at 3 mm. The general trend for larger  $\tau_0$  in the 3 mm light curves as compared with the 1 mm ones is shown in Fig. 3, where  $\tau_{0,3}$  was computed from data covering the same time period as the one for the 1 mm data, see also Table 1.

To summarise, we find that, in general, the variability of total flux millimetre emission in radio-loud AGN is more prominent on short time-scales as compared to that on the longer time-scales when going from 1 mm to 3 mm observing wavelengths. Additionally, the variability also shows larger fractional variability amplitudes and shorter time-scales at 1 mm as compared to 3 mm. These observations are consistent with the assumption that the shorter wavelength emission originates at smaller and more violently variable regions. This is in agreement with models that attribute the jet variability to turbulent processes with cell sizes becoming smaller towards shorter wavelengths (e.g., Marscher 2014).

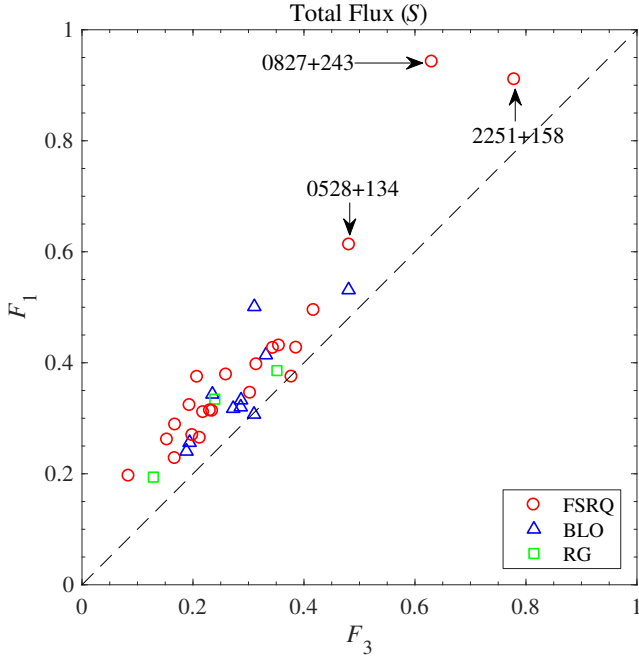


**Figure 2.** Fractional variability ( $F$ , see Table 1) of 1 mm flux versus those at 3 mm for every source in the variable sample. The 3 mm values of  $F$  shown here are those computed for the common time period of the 3 and 1 mm data, i.e. December 2009 to August 2014. Outliers of the distribution of points in this plot are labeled by their corresponding source name.

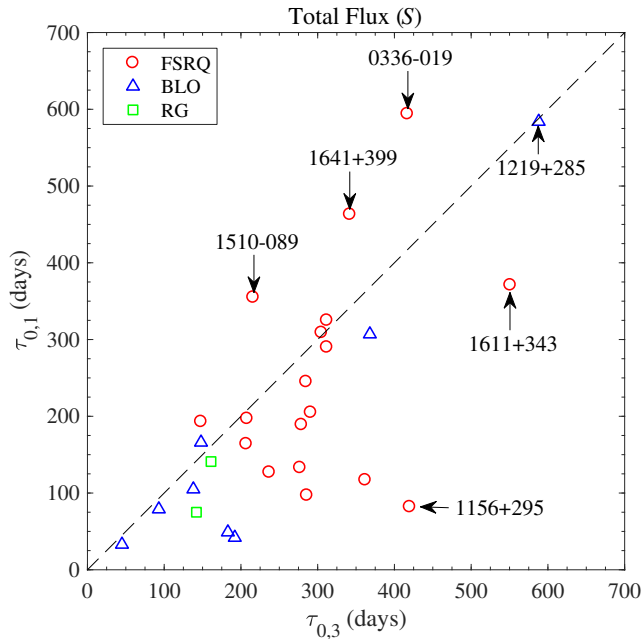


**Figure 3.** Time scale of variability computed from the autocorrelation function ( $\tau_0$ , see Table 1) of 1 mm light curves of every source in the sample versus the corresponding 3 mm value of  $\tau_0$ . The 3 mm values of  $\tau_0$  shown here are those computed for the common time period of the 3 and 1 mm data, i.e. December 2009 to August 2014. Outliers of the distribution of points in this plot are labeled by their corresponding source name.

### 3.2 Spectral index

As it can be seen from the light curves in Fig. 11, the 3-to-1 mm spectral indices ( $\alpha$ )<sup>3</sup> are almost constantly negative. This contrasts with what is found at longer centimetre wavelengths, where the spectral index is typically found close to zero; i.e. flat spectra; or positive; corresponding to optically thick spectra (Angelakis et al. 2012; Fuhrmann et al. 2016). This confirms that the spectrum in the short millimetre range is in general optically thin (see also Agudo et al. 2014). Only for a small fraction of sources (namely 0415+379, 0716+714, 0735+178, 0827+243, 0829+046, 1219+285, and 2200+420) the spectral index raises to positive values but (a) never larger than  $\sim 0.2$  and (b) only during brief periods in the proximity of bright total-flux flares. The median spectral index is  $\bar{\alpha} \approx -0.6$  for the source sample (see Table 2), whereas the standard deviation is  $\text{rms}_\alpha \approx 0.2$ ). This implies an average energy index of the emitting particle distribution for the source sample in the range  $\sim 2.2$  to  $\sim 2.4$  (Rybicki & Lightman 1979), provided such distribution follows a power law.

The general optically thin spectrum of sources is also consistent with the time delays between the 3 and 1 mm light curves being compatible with zero for all strongly flaring sources (within the time resolution given by our DCF, not shown here). The latter agrees with standard shock-in-jet models for the most prominent flares in the data Marscher & Gear (1985); Valtaoja et al. (1992). A study of our total flux and polarization data in the framework of these and other models will be presented in further publications including also the analysis of millimetre VLBI polarization data.

The variability analysis of  $\alpha$  also shows clear evidence of strong variability (Table 2). Indeed, the  $\chi^2$  test shows a probability  $> 99.73\%$  for most sources to be variable in spectral index. Only 0316+413 shows a probability slightly smaller than that, but this is  $98.5\%$ , therefore also showing high probability to be variable<sup>4</sup>.

The PSD slopes of  $\alpha$  for each source range from 2.9 (for 1253–055) to  $\sim 0.5$  (for 1730–130), while the entire source sample shows a median PSD value = 1.1, hence showing in general flatter PSD (i.e. more prominent short time-scale of variability as compared to the long time-scale one) than both the 3 and 1 mm total-flux light curves. Indeed,  $\tau_0$  is actually smaller in general for  $\alpha$  than for  $S_3$  and  $S_1$ , respectively (with the median of  $\tau_{0,\alpha} = 45$  days), whereas the fractional variability amplitude of  $\alpha$  shows similar values in general than those for  $S_3$  (i.e. median of  $F_\alpha = 0.27$ ).

The fact that we find a larger fractional amplitude of variability at 1 mm as compared to the 3 mm (see previous section) should affect the spectral index if the variability at both wavelengths is coherent, as it seems to be the case at first sight from Fig. 11. Therefore, for a larger fractional variability amplitude at 1 mm, we expect that for intense flares, the spectral index (and hence the energy index of the emitting particle distribution) should raise to levels higher than

<sup>3</sup> We define the spectral index between 3 and 1 mm as  $\alpha = \ln(S_3/S_1)/\ln(86/229)$ , where  $S_3$  and  $S_1$  are simultaneous 3 and 1 mm (86 and 229 GHz) total flux measurements, respectively.

<sup>4</sup> In this paper, we claim variability from a data train whenever its  $\chi^2$  test gives a probability  $\geq 95\%$ .



those at quiescence, even while staying optically thin (i.e. on negative values). This is exactly the observed effect that is shown for those sources where sufficiently isolated, bright, and well monitored flares were observed at 3 and 1 mm during the course of our monitoring, e.g. 0528+134, 0735+178, 0827+243, 1226+023, 1611+343, 2230+114, 2251+158. This spectral hardening in bright flares indicates that the spectrum of the newly injected electron distribution responsible for the emission is harder than the quiescent one, and such that the spectral changes are visible in the short mm range, mostly unaffected by opacity effects.

### 3.3 Variability of the linear polarisation degree

Strong variability of the linear polarisation degree ( $m_L$ ) with time is also quite noticeable from Fig. 11 for almost all sources. Inspection of these plots shows that the properties of  $m_L$  variability are notably different from those of total flux, and also that the variability amplitude of  $m_L$  is higher at 1 mm than at 3 mm. This is formally demonstrated from the variability analysis of  $m_L$ , see Table 3 and paragraphs below.

At 3 mm, the values of  $m_L$  range from  $\sim 0\%$  (as observed for many sources, see Fig. 11) up to  $\sim 15\%$  (for 0954+658 and 1055+018). The median  $m_L$  for the entire source sample  $\bar{m}_L \approx 3\%$ . At 1 mm,  $m_L$  ranges from  $\sim 0\%$  to  $16\%$  (for 1222+216 and 1253-055) and the entire source sample has a median  $\bar{m}_L \approx 6\%$ . The comparison of these statistics at both wavelengths suggests a general higher degree of polarisation at 1 mm as compared to the one at 3 mm. This result is not biased by the fact that the 3 mm and 1 mm data trains cover different time periods. Indeed, the same effect was reported before for a much larger source sample measuring  $m_L$  simultaneously at 3 mm and 1 mm at a single epoch (Agudo et al. 2014). This is confirmed again by the new data set presented here through the analysis of the ratio of 1 to 3 mm degree of polarization made for every single simultaneous observation, see next section.

At 3 mm, almost all sources are variable in  $m_L$  according to the  $\chi^2$  test with probability  $> 99.73\%$  ( $P = 95\%$  for the case of 0430+052), see Table 3. Only 0316+413 is an exception and cannot be claimed to be variable in  $m_L$  with the current data set. At 1 mm most of the sources (i.e. 24) are variable in  $m_L$  at 1 mm with  $P > 95\%$ . The remaining 1 mm sources may well also be variable in  $m_L$ , but a formal test does not give significant results due to fewer data points and the generally higher measurement errors at 1 mm.

The typical (median) PSD slopes of  $m_L$  data trains at 3 and 1 mm are 1.3 and 0.8, respectively, which are significantly smaller values as compared to those for the total flux ones. This points out a more prominent short time-scale of  $m_L$  variability than the long time-scale one as compared to the total flux variability, which applies for both the 3 and the 1 mm data. However, unlike for the total flux behaviour, for  $m_L$  the  $\beta_1$  values only show a rather weak trend to cluster at significantly smaller values as compared to the  $\beta_3$  ones, Fig. 4. The main reason for the weakening of this trend for  $m_L$  is the difference in time-range and time sampling for some sources that appear as outliers in Fig. 4.

The fractional variability amplitude of  $m_L$  at 3 mm, with median  $\tilde{F}_3 = 0.53$ , show typical values larger than those for the total flux in general. However, at 1 mm, the fractional

variability amplitudes of  $m_L$ , although with a similar median ( $\tilde{F}_1 = 0.52$ ), are systematically smaller as compared to the 3 mm ones (Fig. 5). Our definition of  $F$  (see Appendix A) accounts for both the mean squared error of every data train, which is subtracted from the variance of such data train. The 1 mm  $m_L$  errors are rather large (Fig. 11), therefore probably decreasing the values of  $F$ . This may lead to a systematic underestimation of the  $F$  values resulting from the measurement errors being systematically higher at 1 mm than at 3 mm. Although this is a hypothesis that cannot be tested with the current data, we speculate that in analogy with the spectral behaviour of the total flux, the fractional variability amplitude a 1 mm should show larger values in general than at 3 mm. However, the current data actually show the opposite effect, with  $F$  at 1 mm showing systematically smaller values than those at 3 mm, see Fig. 5. Again, we attribute this behaviour to the larger relative  $m_L$  errors at 1 mm, and not to the intrinsic properties of the  $m_L$  variability at 1 mm.

The time scales of variability of prominent peaks of  $m_L$ , characterised by  $\tau_0$ , are longer for the 3 mm measurements ( $\bar{\tau}_0 = 171$  days) as compared to the 1 mm ones ( $\bar{\tau}_0 = 45$  days). These numbers are smaller than those characterising the time scale of total flux variability, therefore providing an additional piece of information in support of the faster time scale of linear polarisation variability as compared to the total flux, both for 3 and for 1 mm. The effect of more rapid variability at the shortest wavelength detected by  $\tau_0$  (also observed for the total flux variability behaviour), is also well reproduced in Fig. 6, where we compare  $\tau_0$  at 3 and 1 mm for every given source with enough  $m_L$  data for the variability analysis.

In summary, we have found that  $m_L$  measured at 1 mm is larger in general than at 3 mm. The variability of linear polarisation degree is significantly faster in prominent flares at 1 mm as compared to 3 mm, and it is also more prominent on the shorter time scales studied in this work than on the longer ones as compared to the total flux. These results are again consistent with a jet model where the bulk of the millimetre emission is produced by different independent inhomogeneity (or turbulence) cells evolving in the jet with different configuration of the magnetic field. In this way, more rapid variability would be observed in  $m_L$  than in total flux, since the total flux emission is not affected by emission cancellation of orthogonal polarisation components. Moreover, the fact that the 1 mm polarisation is larger than at 3 mm implies that the average magnetic field is better ordered in the 1 mm emission regions, which because of their smaller size they produce more rapid variability than at 3 mm.

### 3.4 Ratio of 1 to 3 mm degree of polarisation

Agudo et al. (2010) found that the linear polarisation degree measured at a single epoch at 3 mm was, in median, a factor of  $\sim 2$  larger than the one measured at 2 cm for a large sample of 71 AGN (dominated by blazars). A similar result was found by Agudo et al. (2014), who reported the single epoch 1 mm linear polarisation degree of a sample of 22 sources to be a factor  $\sim 1.7$  larger than that at 3 mm for a smaller subsample of 22 sources for which the  $m_{L,1}/m_{L,3}$  coefficient was estimated from strictly simultaneous data at both wavelengths. This evidence was used in support of claims that the magnetic field is progressively better ordered in the

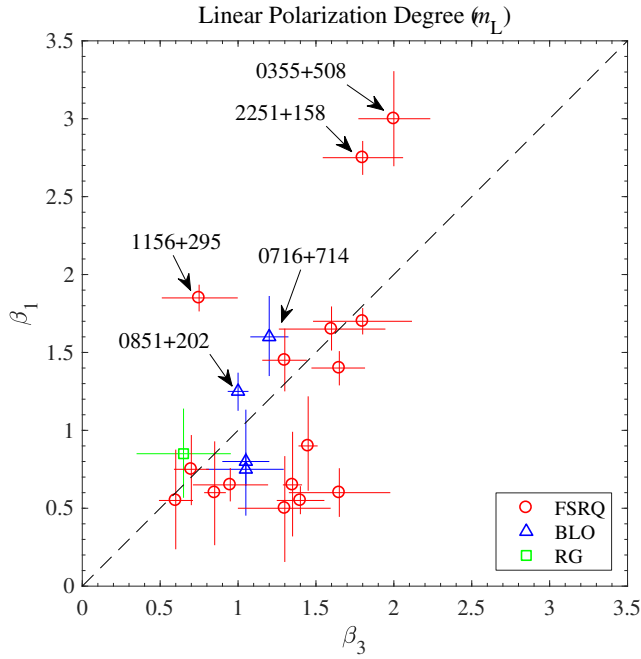


**Figure 4.** Same as Fig. 1 but for  $m_L$ .

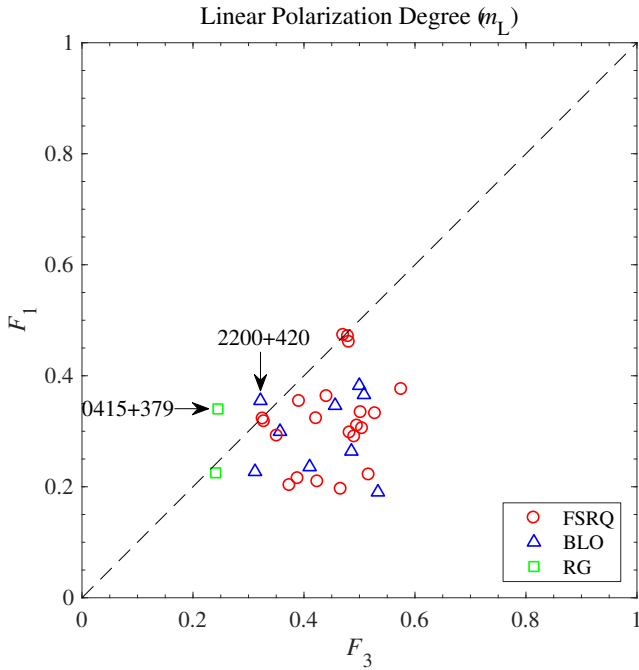


**Figure 5.** Same as Fig. 2 but for  $m_L$ .

blazar jet regions responsible for the emission at progressively smaller millimetre wavelengths (Agudo et al. 2014).

The new database that we present in this work offer the possibility of a similar study, but this time using a large number of measurements per source and exploring the time variability of the  $m_{L,1}/m_{L,3}$  ratio, see Fig. 11. Table 4 shows the statistical variability analysis of  $m_{L,1}/m_{L,3}$ . The 36 sources showed maxima of  $m_{L,1}/m_{L,3}$  ratios ranging from 1.7 (for 2200+420) and 7.4 (for 1219+285), and minima ranging from 0.3 (for 0954+658) and 2.3 (for 0430+052). The me-

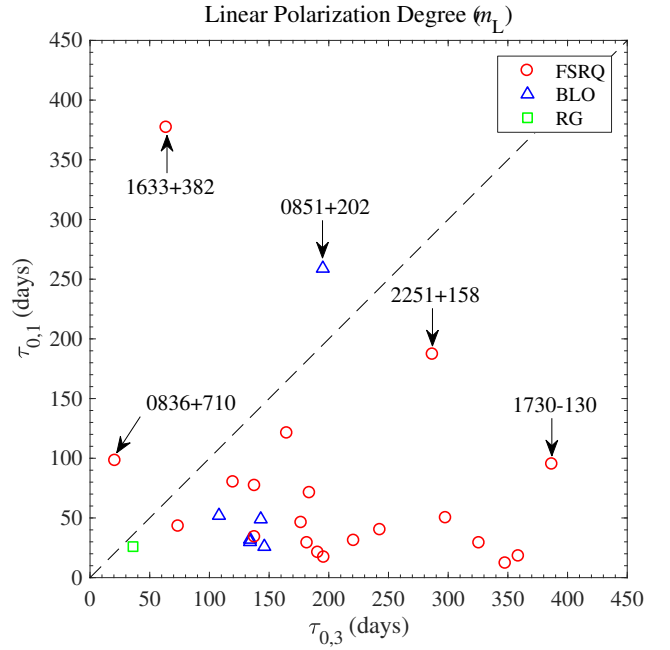


**Figure 6.** Same as Fig. 3 but for  $m_L$ . Two outliers, 1730–130 and 2200+420, are excluded from the selected scale of the plot, see Table 3.

dian values of  $m_{L,1}/m_{L,3}$  for every source range from 1.0 and 3.9, with typical (median of the median) values around 2.6. The latter number confirms that in general, the 1 mm linear polarisation degree is higher than the 3 mm one for AGN jetted sources. Once again, we note that these are numbers that characterise the relatively small population of sources for which we could perform the variability study. However, every one of these sources show different properties with regard to their  $m_{L,1}/m_{L,3}$  behaviour, see Fig. 11 and Table 4.

The variability study concentrates on 29 out of the 36 sample sources for which we have more than 9  $m_L$  measurements with  $\text{SNR} > 1$  at both 3 and 1 mm (Table 4), a condition for us to make the variability study. Among these 29 sources, 10 of them show  $> 95\%$  probability to be variable according to the  $\chi^2$  test. Once again, the large  $m_L$  uncertainties at 1 mm do not allow to ensure variability of the  $m_{L,1}/m_{L,3}$  fraction for a larger fraction of the sources, although that variability is probably a property of all AGN radio loud jets as well.

### 3.5 Variability of linear polarisation angle

The linear polarisation angle ( $\chi$ ) is also found to vary very prominently at both 3 and 1 mm in all sources of the sample, see Fig. 11. This Figure also shows the good (general) correspondence of the  $\chi$  evolution curves at both wavelengths on the long time-scales (of months/years), although on the short time-scales (of weeks), such correspondence is somehow weakened. Indeed, Table 5 shows that all sources for which we had enough measurements to perform the  $\chi^2$  test, are variable at the  $P > 99.73\%$  confidence level.

The  $\chi$  variability found in the source sample shows PSD slopes as flat as  $\beta_3 = 0.5$  at 3 mm (for 0735+178), and as steep as  $\beta \approx 3.0$  (e.g. for 2230+114 and 2251+158) at both wavelengths. The median values of  $\beta$  of the  $\chi$  data trains

are 2.1 at 3 mm, and 1.8 at 1 mm. These similar ranges of values of the PSD slopes at both wavelengths for the source population are also reflected in the one to one comparison for every given source in Fig. 7.

The fractional variability amplitude of  $\chi$  is very similar in general at both 3 mm and 1 mm, with median  $\sim 0.5$  at both wavelengths. Such a good correspondence, also illustrated by the limited spread of the cloud of points on Fig. 8, is not surprising taking into account the good match of the 3 mm and 1 mm  $\chi$  evolutions on the long time scales shown in Fig. 11. Even if there is more (either intrinsic or artificial) short time scale of variability on the 1 mm data, the definition of the fractional variability amplitude (Section 3) makes the scatter on the short time scales to be compensated by the larger mean measurement uncertainties.

The auto-correlation function is however more sensitive to changes of the time-scale of variability at different wavebands, irrespective of the measurement error. Therefore, Table 5 shows significantly shorter  $\tau_0$  time scales of variability of  $\chi$  for the 1 mm (with median = 102 days) as compared to those at 3 mm (with median = 281 days), see also Fig. 9. Together with  $\tau_0$ , we also computed the minimum time for the linear polarisation angle to rotate in every source by  $180^\circ$  and  $90^\circ$ , see Table 5. For 3 mm, we find that 33 out of 36 sources showed at least one  $\chi$  rotation by  $\geq 90^\circ$ , whereas 21 of the 36 sources showed at least one  $\geq 180^\circ$  rotation. For 1 mm, the number of sources showing large rotations are similar. At this wavelength, 32 sources showed at least one  $\chi$  rotation by  $\geq 90^\circ$ , and 25 sources showed at least a  $\geq 180^\circ$  rotation, which seems to suggest that large  $\chi$  rotations is a phenomenon probably inherent to a majority of radio-loud AGN jets. The typical time scales of the  $\geq 180^\circ$  swings range from medians of 81 days at 1 mm, to 147 days at 3 mm, although very different time scales can be found in every particular source (Table 5). Indeed, the standard deviations on the distribution of time scales of  $\geq 180^\circ$  rotations are 208 and 368 days at 1 and 3 mm respectively. This large scatter accounts both for cases of long time scales of  $\geq 180^\circ$  rotations as large as a year or more (e.g. 0829+046 or 1611+343), or rotations in time scales as short as several weeks (e.g. 2251+158), see Fig. 11 and Table 5. Much faster swings are routinely observed in the optical range (e.g., Blinov et al. 2016a,b), where sources may rotate by  $> 180^\circ$  in time scales of a few days (e.g., Marscher et al. 2008; Abdo et al. 2010; Blinov et al. 2016a,b). However, our time sampling does not permit to check if those fast swings also happen in the millimeter bands.

### 3.6 Misalignment between linear polarisation and jet position angles

The prominent polarisation angle variability that characterizes most of our sources causes  $\chi$  to be, in general, rarely closely aligned with the position angle of the inner jet (see Fig. 11). This explains why previous large single-epoch millimetre-polarimetric surveys (Agudo et al. 2010, 2014) did not find clear signs of  $\chi$  aligning parallel (or perpendicular) to the jet position angle, as predicted by axial-symmetric two-dimensional jet-models with the magnetic fields oriented predominantly perpendicular (or parallel, respectively) to the jet (e.g., Lyutikov et al. 2005; Cawthorne 2006). Rather, the misalignment between the linear polar-

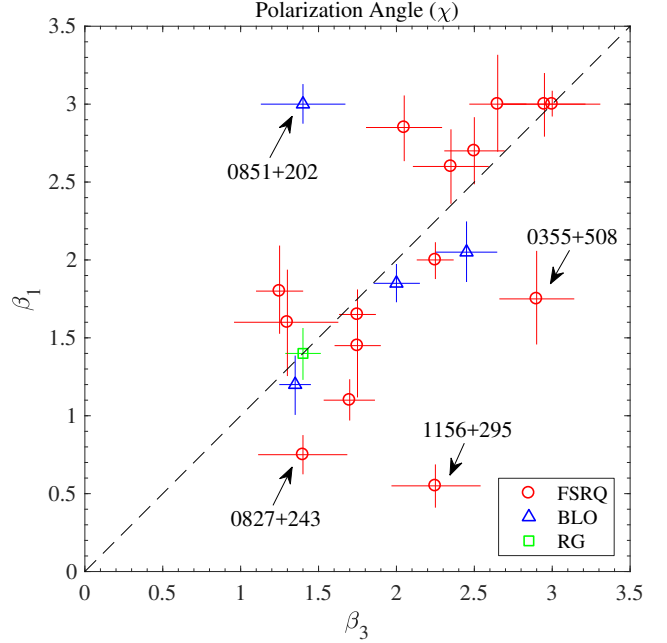


Figure 7. Same as Fig. 1 but for the linear polarisation angle.

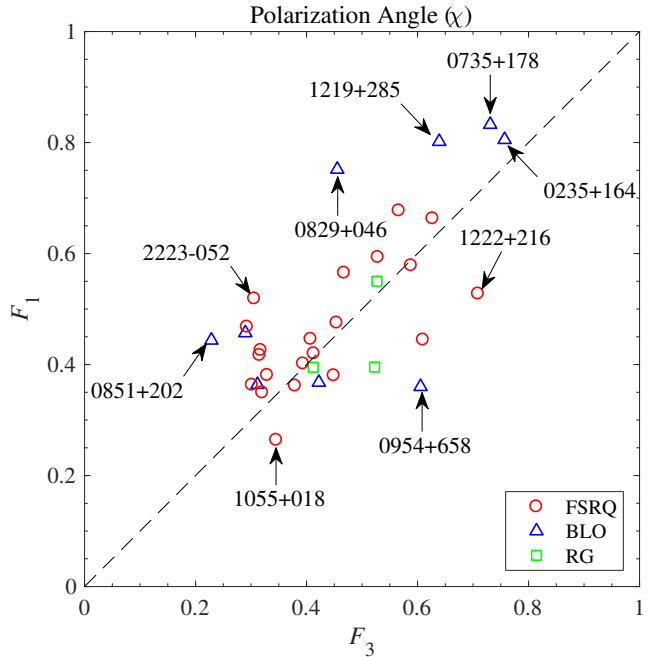
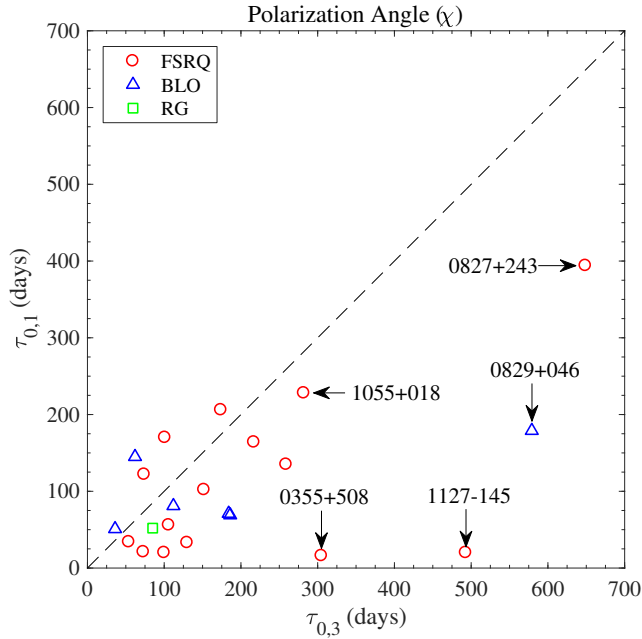


Figure 8. Same as Fig. 2 but for the linear polarisation angle.

isation angle and the jet position angle was shown to take essentially any possible value within the first quarter of the circle for the entire source sample, quasars and BL Lac objects. This is a clear sign of polarisation emission in AGN jets having a remarkable departure from two-dimensional structure.

The new 3 and 1 mm data sets of  $\chi$  presented here are an order of magnitude larger than previous similar millimetre studies (Agudo et al. 2014, 2010). For calculating the distribution of the misalignment angle  $|\chi - \phi_{\text{jet}}|$ , in most



**Figure 9.** Same as Fig. 3 but for the linear polarisation angle. Two outliers, 0235+164 and 0716+714, are excluded from the selected scale of the plot, see Table 5.

of the cases we take as a measurement of the jet position angle ( $\phi_{\text{jet}}$ ) the averaged values given by Jorstad et al. (2017, *ApJ* in press) from sequences of 7 mm VLBI images taken from 2007 to 2014 by the VLBA-BU-BLAZAR Monitoring Program<sup>5</sup>. However, the 0235+164 value is not given by Jorstad et al. (2017, *ApJ* in press) and we measured it from the 7 mm VLBI image on the 23th of October 2016 provided by the VLBA-BU-BLAZAR program. For 0355+508, a source not included in Jorstad et al. (2017, *ApJ* in press),  $\phi_{\text{jet}}$  was taken from the 3 mm VLBI image obtained in May 2010 as reported by Molina et al. (2014).

Our new histograms of  $|\chi - \phi_{\text{jet}}|$  (Fig. 10) confirm the previous results by Agudo et al. (2010, 2014) only for quasars. However, BL Lac objects show a remarkable tendency to cluster at small misalignment angles, i.e.  $\chi$  closely aligned with  $\phi_{\text{jet}}$  (like expected e.g. for jet emission dominated by plane perpendicular shock waves or by toroidal homogeneous magnetic fields, e.g., Wardle et al. 1994; Gabuzda et al. 2000; Lister 2001). Radio galaxies, show a flatter distribution similar to the one of quasars, but with a remarkable deficit of 3 mm data at small misalignment angles that is not present on the 1 mm data. We speculate that this behaviour is produced by the small number of radio galaxies in the sample (only three), that by chance, do not seem to cover the small misalignment region during the time span of our observations. In further studies covering significantly broader time ranges we will test this hypothesis.

Previous work studying the polarisation properties of the cores of VLBI images report contradicting results on which regard to the alignment of the linear polarisation with the jet position angle. In particular, Gabuzda et al. (2000)

observed the polarisation angle of the 6 cm VLBI cores of a sample of BL Lac objects to align predominantly either parallel or perpendicular to the jet position angle. Lister (2001) found the cores of both quasars and BL Lac objects on a sample of 32 blazars observed with 7 mm VLBI to show a strong tendency to align their polarisation angles parallel to the jet position angle. Using a larger sample of 177 sources observed with 6 cm VLBI, Pollack et al. (2003) reported a strong tendency of the polarisation angle of the 6 cm VLBI cores of a large sample of 177 AGN to align perpendicular to the jet position angle in short jets. No preference was found for BL Lac objects for the alignment of their polarisation angle with regard to the jet axis. Later, Lister & Homan (2005), through their 2 cm VLBI observations of a big sample of 133 MOJAVE sources, found a remarkable tendency for BL Lac objects to cluster at small misalignment angles, whereas quasars showed a flatter distribution of misalignment angles. The apparent contradiction of the results from these studies and ours, that cannot be explained in its entirety by opacity effects, is again consistent with the remarkable variability of the polarisation angle shown in Fig. 11 and Table 5.

The behaviour of BL Lac objects shown by Fig. 10 is dominated by 7 of the 11 BL Lac objects in the sample (i.e. 0219+428, 0829+046, 0851+202, 0954+658, 1101+384, 1219+285, and 2200+420), that seem to prefer to orient  $\chi$  at small angles with regard to the 7 mm jet position angle, whereas the remaining 4 sources do not have a clear preference for the orientation of  $\chi$ . The fact that this did not appear on our previous Agudo et al. (2010, 2014) surveys, with a far larger number of sources measured at a single epoch, may mean that these 7 BL Lac objects may be special with regard to the entire BL Lac class, or that we caught them in particularly quiescent states with regard to  $\chi$  variability. The latter hypothesis will be testable by the analysis of the data on a longer time baseline, and by direct comparison with the polarimetric 7 mm VLBI image sequences accumulated by the VLBA-BU-BLAZAR Monitoring Program (Jorstad & Marscher 2016; Jorstad et al. 2017, *ApJ* in press)<sup>6</sup>. Note that something similar than found for BL Lac objects is also observed for a small number of quasars, e.g. 0336-019, 0836+710, 1222+216, 1226+023 (in this case with  $\chi$  preferentially oriented at  $\sim 90^\circ$  of  $\phi_{\text{jet}}$ ), and 1641+399, which may be indicating that there are periods when relativistic jets in AGN show their two dimensional character more prominently, perhaps when they are not much affected with dynamic inhomogeneities in their flow.

The polarisation variability behaviour that we report in this paper suggests that there are still some other ingredients, apart from non-axisymmetry, producing a non-alignment of  $\chi$  and  $\phi_{\text{jet}}$  that we report for a majority of sources (23, out of the total 36). In particular, the faster variability of linear polarisation degree with regard to the total flux one reported above indicates that there is in general more than one single dynamical polarisation component driving the observed emission of the sources. This is evident from the sequences of 7 mm VLBI polarimetric images of the VLBA-BU-BLAZAR Program.

<sup>5</sup> <http://www.bu.edu/blazars/VLBaproject.html>

<sup>6</sup> <https://www.bu.edu/blazars/VLBaproject.html>



The presence of some level of structure in polarisation is known since long ago (e.g. Burn 1966), since it was needed to explain the low polarisation degrees of relativistic jets in AGN as compared to the theoretical expectation ( $\sim 70\%$  for optically thin synchrotron emission of AGN jet plasmas with ordered magnetic field), see Burn (1966); Rybicki & Lightman (1979); Marscher (2014). To decrease  $m_L$  from  $\sim 70\%$  to the average  $\sim 6\%$  at 1 mm that we report in this paper, and under the assumption of a certain level of turbulence in the plasma,  $\sim 150$  turbulent cells are needed (Marscher 2014), which would produce a random behaviour of the resultant polarisation angle. The  $\chi$  variability that we report in Fig. 11 does not appear to be totally random in general, which suggests that there is a significantly smaller number of competing dynamical polarisation components governing the main polarisation behaviour on the top of the lower layer of plasma turbulence. Indeed a small number of such independent dynamical polarisation components (i.e. around 2 or 3, as usually seen on ultra-high resolution VLBI images of AGN jets, e.g. Attridge et al. 2005; Martí-Vidal et al. 2012; Molina et al. 2014; Hada et al. 2016) could reproduce any  $\chi$  behaviour as those shown in Fig. 11. The fact that we do not see an integrated polarisation degree much larger than  $\sim 15\%$  suggests that this is about the maximum degree of polarisation of every one of these most prominent polarisation components (see references above). This supports the idea of an additional scale of turbulence smaller than the size of the emission components usually seen on jet VLBI images.

This is again compatible with a model of jets that is mainly driven by a combination of turbulence, perhaps on different scales, and evolving shocked plasma regions. Turbulent magnetic fields are an ideal scenario for magnetic reconnection (e.g. Sironi et al. 2015, and references therein), which we speculate that should also play a role on the variability properties of the total flux and polarisation of AGN jets, even perhaps with some level of feedback with regard to the production of turbulence.

### 3.7 Rotation measure between 3 and 1 mm

For estimating the observer's-frame rotation measures (RM), we used, the data from every single epoch for which we had simultaneous measurements of  $\chi$  both at 3 and 1 mm, see Fig. 11. The errors in the determination of RM are dominated by the uncertainties on the measurements of  $\chi$  at 1 mm which are  $\sim 10^\circ$ , therefore implying errors  $\sim 2 \times 10^4 \text{ rad m}^{-2}$  in RM. Indeed, this is the median error of all our computations of RM (for the entire source sample) shown in Fig. 11, although many particular  $\chi$  measurements at 1 mm affected by larger non systematic uncertainties give much larger RM errors. Because of the large uncertainties of the RM measurements, we do not provide a detailed variability analysis of this variable, although we can provide constraints about its typical values.

Based on the statistics shown in Table 6, the estimates of RM variations that we report lie  $\lesssim 10^5 \text{ rad m}^{-2}$ , which is about an order of magnitude larger than the typical RM detected by Hovatta et al. (2012) in the large MOJAVE sample (see also Gabuzda et al. 2015; Kravchenko et al. 2017, for studies over smaller source samples). Although not frequent, values  $\sim 10^5 \text{ rad m}^{-2}$  for the RM in AGN jets are not

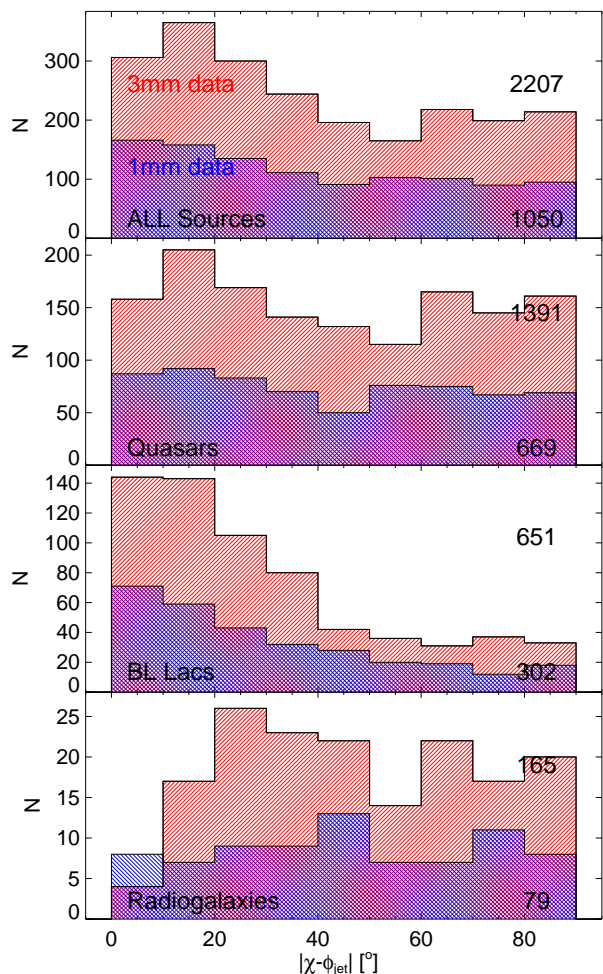


**Figure 10.** Histograms of the misalignment between the jet position angle ( $\phi_{\text{jet}}$ ) and all linear polarisation angle measurements for the entire source sample, quasars, BL Lac objects, and radiogalaxies at both 3 and 1 mm. Numbers displayed to the right indicate the number of measurements for every distribution. The  $\phi_{\text{jet}}$  measurement is taken in most of the cases from Jorstad et al. (2017, ApJ in press). Only the measurements of 0235+164 and 0355+508 were taken from a different source, see text.

unusual (Hovatta et al. 2012), and even seem to be typical in radio-galaxies (e.g., Zavala & Taylor 2004; Gómez et al. 2008, 2011).

However, the  $\sim 10^5 \text{ rad m}^{-2}$  upper limit is about two orders of magnitude smaller than the high RM reported by Martí-Vidal et al. (2015) in the gravitationally lensed AGN PKS 1830–211 through ALMA measurements from up to four sky wavelengths ranging from 3 to 1 mm. Because we only measured  $\chi$  at two wavelengths, and therefore we cannot unambiguously solve for the  $\pi$  ambiguity affecting the RM, our data do not allow us to give a certified explanation about the apparent mismatch between Martí-Vidal et al. (2015) observations and ours. Such mismatch would be solved if a rotation of a multiple of  $\sim 180^\circ$  between the 3 and 1 mm measurements of  $\chi$  would be applied, which would be allowed to overcome a possible  $\pi$  ambiguity. In this case, the corresponding RM would be a mul-

tuple of  $\approx 3 \times 10^6 \text{ rad m}^{-2}$ , which would be more consistent with the measurements by [Martí-Vidal et al. \(2015\)](#). However, the good general match of  $\chi_3$  and  $\chi_1$  shown in Fig. 11 suggests that it would be unlikely that either all or a fraction of sources need such a rotation.

An ongoing dedicated program to measure high precision RM with 6 millimetre wavelengths at the IRAM 30 m Telescope includes some of the sources. We hope this program will provide robust answers regarding this topic. If the low ( $\lesssim 10^5 \text{ rad m}^{-2}$ ) RM regime is confirmed for the sample, this may support the possibility of the particular character of PKS 1830–211 with regard to its large Faraday rotation will be evidenced. Although it is certain that PKS 1830–211 is a high redshift object ( $z = 2.5$ ), which makes the mm wavelengths observed by [Martí-Vidal et al. \(2015\)](#) to be shifted to the short sub-millimeter range, this does not explain the apparent mismatch in RM with all sources. The POLAMI sample also includes high-redshift sources, i.e. 0528+134 (at  $z = 2.1$ ) and 0836+710 (at  $z = 2.2$ ), but all their RM measurements are still consistent with values  $\lesssim 10^5 \text{ rad m}^{-2}$ . Alternatively, the high angular resolution observations of PKS 1830–211 made with ALMA may also play a role on removing some polarisation smearing that may affect the POLAMI single dish observations.

### 3.8 Relation between total flux, linear polarisation degree, and polarisation angle variability

Inspection of Fig. 11 makes it very difficult to find any noticeable relation of the variability in total flux with that of the linear polarisation degree and polarisation angle both at 3 mm and 1 mm for any of the sources in the sample. Each of these three variables (i.e.  $S$ ,  $m_L$ , and  $\chi$ ) seems to follow a complex and independent evolution from each other. To be sure about this, we made a formal cross-correlation analysis by using the DCF defined in Appendix A. The result of the cross-correlations of all  $S$ ,  $m_L$ , and  $\chi$  variables of all sources, at both observing wavelengths, did not show any single correlation peak with a significance larger than 99.73, therefore confirming that correlation of  $S$ ,  $m_L$ , and  $\chi$  is definitely not a general property of the millimetre wave emission of relativistic jets in AGN.

This result may appear surprising if one takes into account that, in origin, the polarised emission of every single emission zone should be directly tied to that of the total flux through the magnetic field in such zone. For a single zone emission system, that should lead to a coherent time evolution in  $S$ ,  $m_L$ , and  $\chi$  all along the spectrum. However, the fact that we actually observe a radically different behaviour implies that, in general, the millimetre emission in AGN relativistic jets is driven by at least two (probably more) emission components.

However, there are particular sources for which particular time ranges may reveal a coherent behaviour on  $S$ ,  $m_L$ , and  $\chi$ . This is e.g. the case of 3C454.3 that in the time between mid 2011 and mid 2012 showed a period of exceptionally weak total flux, high polarisation fraction, and stable polarisation angle at a value very close to the jet position angle, see Fig. 11. In rare cases like this, the emission may be dominated by a single region, and therefore perhaps could be well reproduced by a simple one-zone model.

This seems to be the case for 3C454.3, that during the intriguing event mentioned above seems to be dominated by the highly polarised emission of a single traveling jet component detected in the 7 mm VLBI images of the VLBA–BU-BLAZAR Monitoring Program (see [Jorstad et al. 2013](#); [Jorstad et al. 2017](#), [ApJ in press](#)).

We also looked for signs of periodic behaviour in the  $S$ ,  $m_L$ , and  $\chi$  time evolutions at both 3 and 1 mm for all sources by analyzing their ACF. No clear sign of such periodicity was revealed by the data on any of the variables during the time spanned by our observations.

## 4 SUMMARY AND CONCLUSIONS

We find that all sources in the sample are highly variable in total flux at both 3 and 1 mm. The same is found for the spectral index, that is found to be optically thin between these two wavelengths, except in some specially prominent flares (not all of them), and for short time-scales as compared to the duration of the flares. Therefore, although a small portion of the millimetre emission of the source sample might be affected by opacity effects even in non flaring states, we can safely assume that such opacity effects will not be the most dominant cause of the behaviour of our sources in general. The total flux variability at 1 mm is found, in general, to be faster, and to have larger fractional amplitude than at 3 mm, which in turn should lead to flatter PSD slopes at 1 mm. This finding is consistent with models of the inner jets where the shortest-wavelength millimetre emission is produced by smaller regions. This fits perfectly in the framework of new models for jet emission variability produced by turbulent processes with turbulence cell sizes becoming smaller as emitting wavelength decreases (see [Marscher 2014](#)). Moreover, the larger fractional amplitude of variability at 1 mm as compared to the 3 mm, together with the observed flattening of the spectrum during total flux increases, evidences that the spectrum of the electron distribution injected in flares is harder than the quiescent one. The injected electron distribution is such that the spectral changes are visible in the short mm range, and mostly unaffected by opacity effects.

Confirming previous results by [Agudo et al. \(2014\)](#), the 1 mm polarisation degree is also found higher in general than the 3 mm one by a median factor of 2.6. As we rule out strong opacity effects, this implies that the magnetic field is better ordered on the shorter wavelength regions as compared to the longer wavelength ones. The linear polarisation degree is also highly variable in general, with the time scales of variability in big flares being significantly faster at 1 mm as compared to the 3 mm one. This is compatible with the total flux emission at the short wavelength being also faster than the longer wavelength one if both the polarised and total flux emission is produced in the same sets of regions. Under the internal turbulence scenario proposed by [Marscher \(2014\)](#), such turbulence would distribute the resultant linear polarisation in a different angle for every one of the turbulence cells, which would result not only in a linear polarisation degree far below the theoretical maximum (as it is the case in our observations), but also in faster variability of the linear polarisation with regard to the total flux, as the data shows from the  $\tau_0$  time-scales.

The polarisation angle at both 3 and 1 mm has also been shown to be highly variable, with most of the sources showing at least one excursion of  $> 180^\circ$  on time scales from a few weeks to a year or more during the course of the observations. This strong variability is a likely explanation for the general lack of relation found between the jet position angle and the polarisation angle of the monitored sources, although there is a minority of targets that show a remarkable tendency to align the polarisation angle either parallel to the jet (for 7 of the 11 BL Lac objects observed plus the quasar 1641+399), or perpendicular (for the case of 4 quasars). The reason for the preferential alignment in these sources remains to be investigated through the analysis of longer monitoring data and their combination with polarimetric VLBI image sequences.

The 3 and 1 mm polarisation angle evolution follow rather well each other, although the 1 mm data shows a clear preference to vary slightly more prominently on the short time scales (of weeks). This might be produced by a mix of intrinsic short-time-scale variability and scatter on the more noisy 1 mm data, though. In both cases, the high amplitude variations of the polarisation angle do not seem to have any direct correlation with the total flux and polarisation degree variability in general. On contrary, the polarisation angle variability seems to follow a rather complex evolution as compared to the total flux, the polarisation degree, and even the jet position angle for each particular source. The latter is, by itself, a sign of non-axisymmetry of the millimeter emission zones of AGN jets. Moreover, the variability on the polarisation degree also do not seem to be directly related to the one of the total flux. All this results together automatically imply that, apart from exceptional events of particular sources (like 3C454.3, pointed out in Section 3.8), the variability of the linearly polarised emission cannot be explained by the time evolution of a single emission component. This is, any single zone model will fail to explain the polarisation behaviour of radio-loud AGN like those represented in the sample. Therefore, the number of emission zones in a model capable of explaining together the total flux and polarisation emission of radio-loud AGN should then be larger than one (probably larger than two in some cases) in order to reproduce the apparently erratic behaviour of  $S$ ,  $m_L$  and  $\chi$ , and their apparent lack of direct relation.

Therefore, in summary, the data rule out single-zone jet models for the standard state of radio loud AGN, and are compatible with general multi-zone non-axisymmetric jet models that involve smaller emission regions for the short wavelength emitting sites, which in turn should also be more efficient in energising particle populations than the long wavelength ones. The data also favours the short wavelength emitting regions to have better ordered integrated magnetic fields in general, with different magnetic field orientation for the different emitting regions dominating the emission at every given observing wavelength.

## ACKNOWLEDGEMENTS

The authors acknowledge the anonymous referee for his/her constructive revision of this paper. We gratefully acknowledge Emmanouil Angelakis (MPIfR, Germany) for his care-

ful revision and useful comments to improve this manuscript. This paper is based on observations carried out with the IRAM 30 m Telescope. IRAM is supported by INSU/CNRS (France), MPG (Germany) and IGN (Spain). IA acknowledges support by a Ramón y Cajal grant of the Ministerio de Economía, Industria y Competitividad (MINECO) of Spain. The research at the IAA-CSIC was supported in part by the MINECO through grants AYA2016-80889-P, AYA2013-40825-P, and AYA2010-14844, and by the regional government of Andalucía through grant P09-FQM-4784. This research has made use of the VLBA-BU-BLAZAR Program database of 7 mm VLBA polarimetric images (Jorstad & Marscher 2016; Jorstad et al. 2017, ApJ in press), and the NASA/IPAC Extragalactic Database.

## REFERENCES

- Abdo A. A., et al., 2010, *Nature*, 463, 919  
 Agudo I., Thum C., Wiesemeyer H., Krichbaum T. P., 2010, *ApJS*, 189, 1  
 Agudo I., et al., 2011a, *ApJL*, 726, L13  
 Agudo I., et al., 2011b, *ApJL*, 735, L10  
 Agudo I., Thum C., Wiesemeyer H., Molina S. N., Casadio C., Gómez J. L., Emmanoulopoulos D., 2012, *A&A*, 541, 111  
 Agudo I., Thum C., Gómez J. L., Wiesemeyer H., 2014, *A&A*, 566, 59  
 Agudo I., Thum C., Molina S. N., Casadio C., Wiesemeyer H., Morris D., Paubert G., Gómez J. L., Kramer C., 2017, *MNRAS*, ???, ??? (Paper I)  
 Aleksić J., et al., 2015, *A&A*, 578, A22  
 Alexander T., 2013, e-print, arXiv:1302.1508  
 Angelakis E., et al., 2012, *JPhCS*, 372, 012007  
 Attridge J. M., Wardle J. F. C., Homan D. C., 2005, *ApJ*, 633, L85  
 Blinov D., et al., 2016a, *MNRAS*, 457, 2252  
 Blinov D., et al., 2016b, *MNRAS*, 462, 1775  
 Burn B. J., 1966, *MNRAS*, 133, 67  
 Cawthorne T. V., 2006, *MNRAS*, 367, 851  
 Edelson R. A., Krolik J. H., 1988, *ApJ*, 333, 646  
 Emmanoulopoulos D., McHardy I. M., Papadakis I. E., 2013, *MNRAS*, 433, 907  
 Fuhrmann L., et al., 2016, *A&A*, 596, A45  
 Gabuzda D. C., Pushkarev A. B., Cawthorne T. V., 2000, *MNRAS*, 319, 1109  
 Gabuzda D. C., Knuettel S., Reardon B., 2015, *MNRAS*, 450, 2441  
 Gómez J. L., Marscher A. P., Jorstad S. G., Agudo I., Roca-Sogorb M., 2008, *ApJL*, 681, L69  
 Gómez J. L., Roca-Sogorb M., Agudo I., Marscher A. P., Jorstad S. G., 2011, *ApJ*, 733, 11  
 Hada K., et al., 2016, *ApJ*, 817, 131  
 Hovatta T., Lister M. L., Aller M. F., Aller H. D., Homan D. C., Kovalev Y. Y., Pushkarev A. B., Savolainen T., 2012, *AJ*, 144, 105  
 Jorstad S. G., et al., 2007, *AJ*, 134, 799  
 Jorstad S. G., et al., 2010, *ApJ*, 715, 362  
 Jorstad S. G., et al., 2013, *ApJ*, 773, 147  
 Jorstad S. & Marscher A., 2016, *Galaxies*, 4, 47  
 Jorstad S. G. et al., 2017, *ApJ* in press  
 Kiehlmann S., et al., 2016, *MNRAS*, *A&A* 590, A10  
 Kravchenko, E. V., Kovalev, Y. Y., Sokolovsky, K. V., 2017, *MNRAS*, 467, 83  
 Lister M. L., 2001, *ApJ*, 562, 208  
 Lister M. L. & Homan D. C., 2005, *ApJ*, 130, 1389  
 Lister M. L., et al., 2009, *AJ*, 137, 3718

- Lyutikov M., Pariev V. I., Gabuzda D. C., 2005, *MNRAS*, 360, 869
- Marscher A. P., 2014, *ApJ*, 780, 87
- Marscher A. P. & Gear W. K., 1985, *ApJ*, 298, 114
- Marscher A. P., et al., 2008, *Nature*, 452, 966
- Marscher A. P., et al., 2010, *ApJ*, 710, L126
- Martí-Vidal I., et al., 2012, *A&A*, 542, A107
- Martí-Vidal I., Muller S., Vlemmings W., Horellou C., Aalto S., 2015, *Science*, 348, 311
- Max-Moerbeck W., Richards J. L., Hovatta T., Pavlidou V., Pearson T. J., Readhead A. C. S., 2014, *MNRAS*, 445, 437
- Molina S. N., Agudo I., Gómez J. L., Krichbaum T. P., Martí-Vidal I., Roy A. L., 2014, *A&A*, 566, A26
- Peterson B. M., Wanders I., Horne K., Collier S., Alexander T., Kaspi S., Maoz D., 1998, *PASP*, 110, 660
- Ramakrishnan V., Hovatta T., Nieppola E., Tornikoski M., Lähteenmäki A., Valtaoja E., 2015, *MNRAS*, 452, 1280
- Rybicki G. B., Lightman A. P., 1979, *Radiative Processes in Astrophysics* (New York: J. Wiley)
- Sironi L., Petropoulou M. & Giannios D., 2015, *MNRAS*, 450, 183
- Pollack L. K., Taylor G. B. & Zavala R. T., 2003, *ApJ*, 589, 733
- Tchekhovskoy A., 2015, in: *The Formation and Disruption of Black Hole Jets*, eds: Contopoulos, I., Gabuzda, D., Kylafis, N., Springer 414, 45
- Thum C., Agudo I., Molina S. N., Casadio C., Gómez J. L., Morris D., Ramakrishnan V., Sievers A., 2017, *MNRAS*, ???, ??? (Paper II)
- Uttley P., McHardy I. M., Papadakis I. E., 2002, *MNRAS*, 332, 231
- Valtaoja E., Terasranta H., Urpo S., Nesterov N., Lainela M., Valtonen M., 1992, *A&A*, 254, 71
- Valtonen M. J., et al., 2016, *ApJ*, 819, L37
- Vaughan S., Edelson R., Warwick R. S., Uttley P., 2003, *MNRAS*, 345, 1271
- Wardle, J. F. C., Cawthorne, T. V., Roberts, D. H., Brown, L. F., 1994, *ApJ*, 437, 122
- Welsh W. F., 1999, *PASP*, 111, 1347
- Zavala R. T., Taylor G. B., 2004, *ApJ*, 612, 749



**Table 1.** Variability analysis for total flux ( $S$ ).

Source	3 mm												1.3 mm									
	$N_{\text{obs}}$	min (Jy)	max (Jy)	ratio	$\hat{S}$ (Jy)	$\sigma_S$ (Jy)	Prob.	$\beta$	$F_{\text{var}}$	$F_{\text{var}}^*$	$\tau_0$ (days)	$\tau_0^*$ (days)	$N_{\text{obs}}$	min (Jy)	max (Jy)	ratio	$\hat{S}$ (Jy)	$\sigma_S$ (Jy)	Prob.	$\beta$	$F_{\text{var}}$	$\tau_0$ (days)
(0)	(1)	(2)	(3)	(4)	(5)	(6)	(7)	(8)	(9)	(10)	(11)	(12)	(13)	(14)	(15)	(16)	(17)	(18)	(19)	(20)	(21)	(22)
0219+428	31	0.30	0.83	2.77	0.54	0.15	>99.73	2.85 [2.51, 3.18]	0.26	0.26	543	543	7	0.30	0.68	2.27	0.49	0.14	<i>a</i>	<i>a</i>	<i>a</i>	<i>a</i>
0235+164	50	0.69	4.68	6.78	1.61	1.27	>99.73	1.55 [1.31, 1.78]	0.57	0.19	172	454	15	0.49	1.35	2.76	0.91	0.24	>99.73		0.26	<i>c</i>
0316+413	59	6.82	21.60	3.17	18.19	2.73	>99.73	2.30 [2.25, 2.35]	0.19	0.13	<i>c</i>	<i>c</i>	29	5.27	10.31	1.96	8.88	1.52	>99.73	1.30 [0.99, 1.60]	0.19	490
0336–019	37	1.03	3.38	3.28	2.25	0.57	>99.73	2.10 [1.98, 2.22]	0.28	0.24	530	417	19	0.59	2.21	3.75	1.31	0.40	>99.73	<i>b</i>	0.31	594
0355+508	76	2.28	7.40	3.25	4.62	1.02	>99.73	1.75 [1.58, 1.92]	0.19	0.17	427	291	35	1.40	3.30	2.36	1.91	0.52	>99.73	1.90 [1.56, 2.24]	0.23	205
0415+379	91	1.66	13.46	8.11	3.70	3.20	>99.73	1.65 [1.46, 1.85]	0.54	0.24	681	161	47	1.04	4.12	3.96	2.44	0.81	>99.73	1.50 [1.40, 1.60]	0.33	141
0420–014	46	1.79	7.91	4.42	4.21	1.16	>99.73	1.90 [1.76, 2.03]	0.24	0.21	318	286	29	0.90	3.29	3.66	2.28	0.57	>99.73	1.30 [0.99, 1.61]	0.26	97
0430+052	26	0.83	5.26	6.34	2.21	1.10	>99.73	<i>b</i>	0.43	0.35	127	142	14	0.80	2.80	3.50	1.37	0.60	>99.73	<i>b</i>	0.39	75
0528+134	68	0.63	5.57	8.84	2.76	1.24	>99.73	2.25 [2.17, 2.33]	0.55	0.48	368	285	26	0.26	2.18	8.38	1.60	0.60	>99.73	1.90 [1.71, 2.08]	0.61	245
0716+714	108	0.66	8.69	13.17	3.78	1.67	>99.73	1.45 [1.33, 1.57]	0.51	0.48	301	93	64	0.52	7.66	14.73	2.87	1.56	>99.73	1.30 [1.05, 1.55]	0.53	79
0735+178	52	0.31	1.08	3.48	0.87	0.21	>99.73	2.05 [1.77, 2.33]	0.31	0.29	805	769	31	0.21	0.90	4.29	0.61	0.18	>99.73	2.35 [2.09, 2.61]	0.32	<i>c</i>
0827+243	73	0.50	4.02	8.04	1.52	1.01	>99.73	1.70 [1.57, 1.83]	0.60	0.63	189	207	42	0.26	3.45	13.27	1.93	1.14	>99.73	1.65 [1.58, 1.72]	0.94	164
0829+046	52	0.36	1.59	4.42	0.70	0.29	>99.73	1.45 [1.31, 1.59]	0.34	0.33	236	192	30	0.22	1.07	4.86	0.53	0.23	>99.73	0.70 [0.39, 1.02]	0.41	42
0836+710	91	0.70	3.21	4.59	1.48	0.57	>99.73	2.65 [2.59, 2.70]	0.34	0.31	743	<i>a</i>	48	0.25	1.54	6.16	0.65	0.29	>99.73	1.35 [1.05, 1.64]	0.40	294
0851+202	92	1.26	9.16	7.27	5.52	1.58	>99.73	2.00 [1.88, 2.12]	0.33	0.27	150	138	57	1.16	5.94	5.12	3.63	1.04	>99.73	0.95 [0.80, 1.09]	0.82	105
0954+658	79	0.75	2.04	2.72	1.36	0.29	>99.73	<i>b</i>	0.21	0.19	111	183	42	0.52	1.37	2.63	0.97	0.23	>99.73	0.60 [0.41, 0.79]	0.24	49
1055+018	61	1.40	5.64	4.03	4.10	1.08	>99.73	2.35 [2.24, 2.46]	0.30	0.30	280	312	38	0.92	4.23	4.60	2.30	0.81	>99.73	2.05 [1.91, 2.19]	0.35	325
1101+384	25	0.30	0.85	2.83	0.50	0.13	>99.73	<i>b</i>	0.23	0.23	45	45	18	0.10	0.58	5.80	0.32	0.11	>99.73	<i>b</i>	0.34	33
1127–145	56	0.86	2.85	3.31	1.64	0.41	>99.73	2.30 [2.18, 2.42]	0.24	0.22	256	237	28	0.43	1.28	2.98	0.72	0.25	>99.73	1.65 [1.43, 1.89]	0.31	127
1156+295	59	0.62	3.07	4.95	1.37	0.63	>99.73	1.85 [1.51, 2.18]	0.42	0.34	328	420	32	0.34	1.54	4.53	0.82	0.35	>99.73	1.30 [1.06, 1.52]	0.43	82
1219+285	33	0.27	0.72	2.67	0.44	0.15	>99.73	0.55 [0.29, 0.81]	0.31	0.31	603	588	17	0.10	0.72	7.20	0.34	0.16	>99.73	<i>b</i>	0.50	584
1222+216	60	0.56	2.58	4.61	1.65	0.37	>99.73	1.95 [1.80, 2.10]	0.24	0.21	278	279	45	0.29	1.82	6.28	1.01	0.34	>99.73	1.05 [0.94, 1.15]	0.37	189
1226+023	83	5.65	28.14	4.98	11.61	5.23	>99.73	2.45 [2.34, 2.56]	0.39	0.26	<i>c</i>	<i>c</i>	53	1.87	8.68	4.64	4.08	1.62	>99.73	2.10 [1.77, 2.44]	0.38	416
1253–055	77	11.10	32.81	2.96	20.71	4.72	>99.73	<i>b</i>	0.22	0.20	418	305	37	6.73	19.11	2.84	12.35	3.20	>99.73	2.05 [1.92, 2.18]	0.27	309
1308+326	54	1.11	2.33	2.10	1.66	0.28	>99.73	2.35 [2.28, 2.42]	0.16	0.17	288	277	35	0.36	1.44	4.00	0.97	0.25	>99.73	1.75 [1.66, 1.84]	0.29	133
1406–076	32	0.55	1.00	1.82	0.75	0.08	>99.73	1.15 [0.80, 1.47]	0.10	0.08	464	148	14	0.23	0.49	2.13	0.36	0.07	>99.73	<i>b</i>	0.20	193
1510–089	53	1.44	5.81	4.03	2.75	1.20	>99.73	<i>b</i>	0.38	0.38	160	216	27	0.80	3.20	4.00	1.89	0.67	>99.73	1.65 [1.56, 1.74]	0.37	355
1611+343	69	1.02	2.70	2.65	2.18	0.43	>99.73	2.25 [2.05, 2.46]	0.24	0.19	<i>c</i>	<i>c</i>	43	0.40	1.52	3.80	1.13	0.28	>99.73	1.20 [0.95, 1.44]	0.32	371
1633+382	76	1.92	8.03	4.18	4.11	1.64	>99.73	1.95 [1.89, 2.00]	0.38	0.36	254	208	48	0.99	5.50	5.56	2.85	1.16	>99.73	1.95 [1.84, 2.06]	0.43	197
1641+399	80	2.65	6.37	2.40	3.65	0.94	>99.73	2.45 [2.27, 2.63]	0.21	0.15	395	342	52	1.09	3.69	3.39	1.76	0.59	>99.73	1.60 [1.37, 1.85]	0.26	463
1730–130	48	2.05	5.97	2.91	3.13	0.82	>99.73	2.30 [2.03, 2.57]	0.22	0.23	668	<i>a</i>	26	0.95	2.92	3.07	1.50	0.56	>99.73	2.05 [1.95, 2.16]	0.31	709
1749+096	62	1.77	5.45	3.08	3.22	1.00	>99.73	1.70 [1.52, 1.88]	0.28	0.29	152	148	44	0.80	3.36	4.20	1.70	0.65	>99.73	1.65 [1.55, 1.76]	0.33	166
2200+420	70	1.77	13.41	7.58	6.98	2.64	>99.73	1.35 [1.07, 1.64]	0.45	0.31	<i>c</i>	<i>c</i>	44	2.85	10.94	3.84	5.59	1.88	>99.73	0.95 [0.82, 1.09]	0.31	307
2223–052	60	0.91	6.49	7.13	4.58	1.75	>99.73	<i>b</i>	0.58	0.42	<i>c</i>	<i>c</i>	29	0.40	2.01	5.03	1.21	0.49	>99.73	2.10 [1.97, 2.23]	0.49	654
2230+114	67	0.99	5.23	5.28	3.43	1.08	>99.73	1.95 [1.87, 2.03]	0.37	0.39	472	362	30	0.62	2.92	4.71	1.34	0.66	>99.73	2.10 [2.01, 2.20]	0.43	117
2251+158	80	2.68	45.19	16.86	24.20	11.53	>99.73	2.25 [2.19, 2.31]	0.68	0.78	458	312	39	0.98	41.37	42.21	24.22	11.56	>99.73	1.85 [1.79, 1.91]	0.31	290
min	25	0.27	0.72	1.82	0.44	0.08	–	0.55 [0.29, 0.81]	0.10	0.08	45	45	7	0.10	0.49	1.96	0.32	0.07	–	0.60 [0.41, 0.79]	0.19	33
max	108	11.10	45.19	16.86	24.20	11.53	–	2.85 [2.51, 3.18]	0.68	0.78	805	769	64	6.73	41.37	42.21	24.22	11.56	–	2.35 [2.09, 2.61]	0.94	709
median	60	2.28	13.41	4.98	6.98	2.64	–	1.90 [1.70, 2.05]	0.28	0.24	318	285	33	1.40	8.68	4.64	12.35	1.56	–	1.60 [1.30, 1.90]	0.33	197
std. dev.	20	3.74	14.99	4.87	9.36	3.56	–	0.54	0.16	0.19	198	160	13	2.39	15.39	16.27	10.53	4.69	–	0.47	0.22	187

Columns are as follows: (0) Source names following the IAU convention as defined in Paper I, where we also give other common source names; (1) number of observations; (2) minimum flux; (3) maximum flux; (4) ratio of maximum to minimum flux; (5) median flux; (6) standard deviation of flux; (7) probability of the source being variable according to  $\chi^2$  test; (8) PSD slope with power-law  $\propto f^{-\beta}$ , for the time period from December 2009 to August 2014, along with 68% confidence intervals (in square brackets); (9) fractional variability amplitude for the entire time range spanned by every data train; (10) same as (9) but for the time period from December 2009 to August 2014; (11) Zero-crossing time scale from autocorrelation function; (12) same as (11) but for the time period from December 2009 to August 2014; (13)–(20) same as (1)–(8) but for 1 mm; (21) and (22) are same as (10) and (12) but for 1 mm, respectively.

<sup>a</sup> Not enough data. Number of data points <10.

<sup>b</sup> Probability of PSD slope <0.05.

<sup>c</sup> No zero-crossing points in ACF.

**Table 2.** Variability analysis for the Spectral Index  $\alpha$ . Columns are same as in Table 1

Source	$N_{\text{obs}}$	min	max	$\tilde{\alpha}$	$\sigma_{\alpha}$	Prob.	$\beta$	$F_{\text{var}}$	$\tau_0$ (days)
0219+428	7	-0.66	-0.18	-0.37	0.17	<i>a</i>	<i>a</i>	<i>a</i>	<i>a</i>
0235+164	15	-0.80	-0.35	-0.59	0.15	>99.73	<i>b</i>	0.25	86
0316+413	29	-0.97	-0.53	-0.76	0.10	98.58	0.60 [0.46, 0.74]	0.08	20
0336-019	19	-1.08	-0.41	-0.62	0.18	>99.73	<i>b</i>	0.25	45
0355+508	35	-1.17	-0.62	-0.89	0.14	>99.73	1.40 [1.09, 1.69]	0.12	196
0415+379	47	-1.07	0.21	-0.46	0.31	>99.73	1.15 [1.05, 1.25]	0.68	169
0420-014	29	-1.40	-0.50	-0.72	0.20	>99.73	1.55 [1.44, 1.66]	0.25	97
0430+052	14	-0.76	-0.28	-0.42	0.15	>99.73	<i>b</i>	0.27	26
0528+134	26	-1.27	-0.38	-0.85	0.27	>99.73	1.55 [1.40, 1.70]	0.30	314
0716+714	64	-1.10	0.07	-0.27	0.20	>99.73	0.60 [0.26, 0.93]	0.60	22
0735+178	31	-0.71	0.00	-0.36	0.16	>99.73	2.30 [2.13, 2.47]	0.35	93
0827+243	42	-1.40	0.23	-0.76	0.42	>99.73	1.70 [1.46, 1.94]	0.62	164
0829+046	30	-1.16	0.09	-0.48	0.31	>99.73	0.95 [0.85, 1.06]	0.59	35
0836+710	48	-1.42	-0.04	-0.79	0.29	>99.73	1.00 [0.87, 1.14]	0.35	40
0851+202	57	-1.05	-0.15	-0.47	0.17	>99.73	0.90 [0.72, 1.07]	0.32	22
0954+658	42	-0.81	-0.04	-0.41	0.18	>99.73	0.90 [0.77, 1.03]	0.41	41
1055+018	38	-1.02	-0.26	-0.57	0.16	>99.73	<i>b</i>	0.19	20
1101+384	18	-1.49	-0.13	-0.58	0.34	>99.73	<i>b</i>	0.60	54
1127-145	28	-1.33	-0.61	-0.95	0.19	>99.73	0.70 [0.47, 0.92]	0.17	21
1156+295	32	-1.23	-0.15	-0.49	0.23	>99.73	1.40 [1.30, 1.50]	0.39	36
1219+285	17	-1.25	0.06	-0.41	0.32	>99.73	<i>b</i>	0.68	40
1222+216	45	-1.34	-0.34	-0.61	0.25	>99.73	0.65 [0.35, 0.95]	0.35	119
1226+023	53	-1.61	-0.54	-0.95	0.22	>99.73	1.80 [1.65, 1.93]	0.18	108
1253-055	37	-0.91	-0.38	-0.66	0.14	>99.73	2.90 [2.78, 3.02]	0.19	412
1308+326	35	-1.15	-0.33	-0.64	0.19	>99.73	2.85 [2.65, 3.06]	0.25	32
1406-076	14	-1.22	-0.52	-0.72	0.16	>99.73	<i>b</i>	0.20	111
1510-089	27	-1.23	-0.35	-0.66	0.21	>99.73	1.35 [1.16, 1.54]	0.30	28
1611+343	43	-1.21	-0.52	-0.78	0.19	>99.73	0.70 [0.47, 0.93]	0.20	191
1633+382	48	-1.07	-0.33	-0.54	0.15	>99.73	1.10 [0.83, 1.36]	0.22	46
1641+399	52	-1.20	-0.49	-0.77	0.14	>99.73	1.10 [1.04, 1.16]	0.16	54
1730-130	26	-1.01	-0.48	-0.76	0.15	>99.73	0.50 [0.30, 0.70]	0.16	457
1749+096	44	-0.93	-0.27	-0.60	0.16	>99.73	1.50 [1.43, 1.57]	0.22	35
2200+420	44	-0.59	-0.00	-0.21	0.13	>99.73	0.60 [0.40, 0.81]	0.47	36
2223-052	29	-1.52	-0.63	-0.88	0.23	>99.73	1.10 [0.83, 1.38]	0.24	36
2230+114	30	-0.94	-0.28	-0.63	0.14	>99.73	0.75 [0.47, 1.04]	0.19	30
2251+158	39	-1.40	-0.03	-0.52	0.29	>99.73	1.35 [1.15, 1.56]	0.53	349
min	7	-1.61	-0.63	-0.95	0.10	–	0.50 [0.30, 0.70]	0.08	20
max	64	-0.59	0.23	-0.21	0.42	–	2.90 [2.78, 3.02]	0.68	457
median	33	-1.16	-0.33	-0.59	0.21	–	1.10 [0.90, 1.40]	0.27	45
std. dev.	13	0.25	0.25	0.18	0.08	–	0.61	0.18	115

**Table 3.** Variability analysis for linear polarization degree( $m_L$ ). Columns are same as in Table 1.

Source	3 mm												1.3 mm											
	$N_{\text{obs}}$	min (%)	max (%)	diff	$\bar{m}_{\text{L}}$ (%)	$\sigma_{m_{\text{L}}}$ (%)	Prob.	$\beta$	$F_{\text{var}}$	$F_{\text{var}}^*$	$\tau_0$ (days)	$\tau_0^*$ (days)	$N_{\text{obs}}$	min (%)	max (%)	diff	$\bar{m}_{\text{L}}$ (%)	$\sigma_{m_{\text{L}}}$ (%)	Prob.	$\beta$	$F_{\text{var}}$	$\tau_0$ (days)		
0219+428	30	1.0	6.5	5.5	2.3	1.3	>99.73	0.55 [0.26, 0.84]	0.41	0.41	33	33	4	4.7	10.6	5.9	8.9	2.5	<i>a</i>	<i>a</i>	<i>a</i>	<i>a</i>		
0235+164	45	0.6	6.0	5.4	2.5	1.2	>99.73	0.50 [0.41, 0.59]	0.42	0.41	229	422	10	1.9	9.2	7.3	4.8	2.2	87.52	<i>b</i>	0.24	<i>c</i>		
0316+413	39	0.4	2.1	1.7	0.9	0.4	42.36	<i>b</i>	0.18	0.17	52	34	9	1.3	5.0	3.7	2.6	1.3	<i>a</i>	2.85 [2.59, 3.11]	<i>a</i>	<i>a</i>		
0336-019	36	0.7	5.6	4.9	3.0	1.2	>99.73	2.10 [1.97, 2.24]	0.41	0.37	213	184	12	4.0	8.4	4.4	5.7	1.5	11.34	<i>b</i>	0.20	71		
0355+508	67	0.6	7.5	6.9	2.3	1.5	>99.73	2.00 [1.77, 2.23]	0.53	0.47	195	221	28	1.5	6.8	5.3	4.2	1.4	53.11	3.00 [2.70, 3.31]	0.20	31		
0415+379	66	0.5	3.2	2.7	1.4	0.6	>99.73	0.65 [0.35, 0.95]	0.25	0.25	41	36	25	1.4	8.7	7.3	3.8	2.2	98.70	0.85 [0.57, 1.14]	0.34	26		
0420-014	45	0.5	5.8	5.3	2.5	1.4	>99.73	0.70 [0.59, 0.81]	0.49	0.51	193	196	23	2.2	11.7	9.5	5.1	2.3	>99.73	0.75 [0.52, 0.97]	0.30	17		
0430+052	19	0.9	3.0	2.1	1.8	0.7	94.87	<i>b</i>	0.23	0.24	219	145	10	2.8	9.3	6.5	5.4	2.2	86.85	<i>b</i>	0.23	<i>c</i>		
0528+134	62	0.5	6.8	6.3	2.1	1.2	>99.73	0.60 [0.33, 0.86]	0.46	0.42	279	120	18	2.2	10.2	8.0	4.8	2.4	97.56	<i>b</i>	0.32	80		
0716+714	107	0.5	8.8	8.3	3.5	2.0	>99.73	1.20 [1.08, 1.32]	0.52	0.51	94	134	46	1.6	11.6	10.0	4.8	2.6	>99.73	1.60 [1.35, 1.86]	0.37	30		
0735+178	49	0.8	7.3	6.5	2.4	1.4	>99.73	0.90 [0.64, 1.16]	0.48	0.49	170	143	16	1.9	9.7	7.8	3.9	2.3	95.79	<i>b</i>	0.26	49		
0827+243	70	0.6	6.5	5.9	2.4	1.3	>99.73	1.45 [1.39, 1.51]	0.47	0.48	227	191	26	1.7	11.6	9.9	5.6	2.6	99.60	0.90 [0.61, 1.22]	0.30	21		
0829+046	50	1.1	9.7	8.6	3.6	2.3	>99.73	1.30 [0.96, 1.64]	0.54	0.53	160	134	16	4.4	14.9	10.5	8.0	2.7	87.91	<i>b</i>	0.19	32		
0836+710	84	0.6	4.8	4.2	2.1	1.0	>99.73	0.85 [0.78, 0.92]	0.39	0.39	46	21	30	1.6	9.3	7.7	4.7	2.3	93.59	0.60 [0.26, 0.93]	0.21	98		
0851+202	92	1.1	12.7	11.6	7.3	2.8	>99.73	1.00 [0.93, 1.07]	0.37	0.36	169	195	48	2.2	14.4	12.2	8.9	3.1	>99.73	1.25 [1.13, 1.37]	0.30	259		
0954+658	79	2.2	14.6	12.4	8.1	2.6	>99.73	1.05 [0.90, 1.20]	0.32	0.31	62	108	36	2.8	12.8	10.0	6.7	2.3	>99.73	0.80 [0.45, 1.13]	0.23	52		
1055+018	60	1.0	14.8	13.8	5.2	3.0	>99.73	1.35 [1.29, 1.41]	0.54	0.44	320	359	34	1.7	12.6	10.9	6.5	2.9	>99.73	0.65 [0.32, 0.99]	0.36	18		
1101+384	25	1.0	5.3	4.3	3.0	1.1	>99.73	<i>b</i>	0.27	0.27	36	36	5	5.0	6.1	1.1	5.3	0.4	<i>a</i>	<i>a</i>	<i>a</i>	<i>a</i>		
1127-145	54	0.9	10.1	9.2	3.0	2.2	>99.73	1.65 [1.36, 1.95]	0.56	0.58	139	138	21	2.4	14.2	11.8	6.4	3.2	>99.73	<i>b</i>	0.38	77		
1156+295	53	0.6	7.4	6.8	3.1	1.7	>99.73	0.75 [0.51, 1.00]	0.50	0.52	277	177	27	1.7	11.0	9.3	5.7	2.3	96.50	1.85 [1.76, 1.93]	0.22	46		
1219+285	31	0.6	6.7	6.1	3.7	1.7	>99.73	0.75 [0.64, 0.87]	0.44	0.46	62	162	11	3.5	13.5	10.0	5.8	3.0	99.67	<i>b</i>	0.35	<i>c</i>		
1222+216	60	1.1	11.7	10.6	7.0	2.3	>99.73	1.65 [1.33, 1.98]	0.35	0.33	359	348	37	2.9	15.7	12.8	7.0	3.0	>99.73	0.60 [0.44, 0.76]	0.32	12		
1226+023	82	0.6	6.5	5.9	3.4	1.2	>99.73	1.30 [1.00, 1.59]	0.32	0.33	101	326	32	1.4	8.1	6.7	3.3	2.0	98.79	0.50 [0.16, 0.83]	0.32	29		
1253-055	76	0.7	12.9	12.2	6.2	3.3	>99.73	1.60 [1.26, 1.95]	0.55	0.47	<i>c</i>	<i>c</i>	32	1.2	15.9	14.7	8.0	3.9	>99.73	1.65 [1.51, 1.80]	0.47	<i>c</i>		
1308+326	52	0.6	7.1	6.5	3.0	1.8	>99.73	1.30 [1.16, 1.44]	0.51	0.50	155	138	26	2.1	14.6	12.5	6.0	3.0	99.07	1.45 [1.25, 1.65]	0.33	34		
1406-076	30	1.0	7.0	6.0	4.0	1.5	>99.73	1.75 [1.48, 2.02]	0.35	0.36	53	196	6	3.1	13.8	10.7	7.0	3.6	<i>a</i>	<i>a</i>	<i>a</i>	<i>a</i>		
1510-089	53	0.6	6.5	5.9	2.6	1.4	>99.73	0.60 [0.49, 0.71]	0.46	0.48	43	74	21	2.1	12.5	10.4	5.6	3.3	>99.73	0.55 [0.24, 0.88]	0.47	43		
1611+343	65	0.5	8.1	7.6	3.6	1.9	>99.73	1.65 [1.47, 1.82]	0.53	0.49	188	165	34	1.9	13.6	11.7	5.4	2.5	>99.73	1.40 [1.29, 1.51]	0.29	121		
1633+382	71	0.4	5.6	5.2	2.5	1.2	>99.73	0.95 [0.71, 1.19]	0.43	0.42	85	64	32	1.9	9.3	7.4	4.6	1.9	84.02	0.65 [0.54, 0.76]	0.21	377		
1641+399	79	0.5	8.6	8.1	3.5	1.6	>99.73	1.80 [1.48, 2.12]	0.43	0.39	363	182	44	1.6	12.4	10.8	4.3	2.5	>99.73	1.70 [1.62, 1.78]	0.35	29		
1730-130	48	0.6	6.5	5.9	2.4	1.5	>99.73	1.50 [1.28, 1.72]	0.50	0.50	538	387	13	1.9	9.2	7.3	3.0	2.1	82.76	<i>b</i>	0.31	95		
1749+096	60	0.4	7.2	6.8	3.3	1.7	>99.73	1.05 [0.80, 1.29]	0.50	0.50	171	146	37	1.5	10.2	8.7	5.2	2.5	>99.73	0.75 [0.64, 0.86]	0.38	26		
2200+420	70	2.4	13.5	11.1	8.1	2.7	>99.73	1.95 [1.63, 2.27]	0.34	0.32	844	465	41	2.6	14.9	12.3	7.5	3.1	>99.73	<i>b</i>	0.36	395		
2223-052	59	0.8	6.9	6.1	2.7	1.5	>99.73	1.75 [1.65, 1.85]	0.48	0.48	328	243	19	1.5	10.3	8.8	4.0	2.8	>99.73	<i>b</i>	0.46	40		
2230+114	63	0.6	6.7	6.1	3.2	1.2	>99.73	1.40 [1.25, 1.55]	0.35	0.35	257	298	22	1.7	8.9	7.2	4.8	2.3	95.53	0.55 [0.46, 0.64]	0.29	50		
2251+158	73	0.6	7.5	6.9	3.2	2.1	>99.73	1.80 [1.54, 2.06]	0.59	0.53	274	287	28	1.7	9.7	8.0	4.7	2.1	>99.73	2.75 [2.64, 2.86]	0.33	187		
min	19	0.4	2.1	1.7	0.9	0.4	–	0.50 [0.41, 0.59]	0.18	0.17	33	21	4	1.2	5.0	1.1	2.6	0.4	–	0.50 [0.16, 0.83]	0.19	12		
max	107	2.4	14.8	13.8	8.1	3.3	–	2.10 [1.97, 2.24]	0.59	0.58	844	465	48	5.0	15.9	14.7	8.9	3.9	–	3.00 [2.70, 3.31]	0.47	395		
median	60	0.6	7.3	6.2	3.2	1.7	–	1.30 [0.95, 1.50]	0.35	0.36	171	165	25	2.1	11.0	9.1	5.6	2.5	–	0.80 [0.65, 0.90]	0.30	45		
std. dev.	19	0.4	3.1	2.8	1.7	0.7	–	0.47	0.13	0.13	162	115	12	1.0	2.7	2.8	1.6	0.6	–	0.80	0.08	101		

POLAMI III: Total flux density and polariz.

**Table 4.** Variability analysis for the polarization fraction  $m_{L,1/3}$ . Columns are same as in Table 1

Source	$N_{\text{obs}}$	min	max	$m_{L,1/3}$	$\sigma m_{L,1/3}$	Prob.	$\beta$	$F_{\text{var}}$	$\tau_0$ (days)
0219+428	4	2.2	4.4	2.4	1.0	<i>a</i>	<i>a</i>	<i>a</i>	<i>a</i>
0235+164	9	0.7	2.7	2.2	0.5	<i>a</i>	<i>a</i>	<i>a</i>	<i>a</i>
0316+413	3	1.1	3.5	3.5	0.9	<i>a</i>	<i>a</i>	<i>a</i>	<i>a</i>
0336-019	12	1.3	3.6	2.4	0.8	19.87	<i>b</i>	0.19	125
0355+508	22	0.7	4.0	1.8	1.0	22.98	<i>b</i>	0.26	40
0415+379	13	0.9	3.4	2.0	1.0	16.60	<i>b</i>	0.56	88
0420-014	22	0.5	4.2	2.1	1.0	>99.73	<i>b</i>	0.04	31
0430+052	6	2.3	6.1	3.9	1.4	<i>a</i>	<i>a</i>	<i>a</i>	<i>a</i>
0528+134	13	0.8	3.4	2.4	0.8	55.31	<i>b</i>	0.26	80
0716+714	44	0.5	3.8	1.5	0.9	85.66	2.40 [2.24, 2.55]	0.24	21
0735+178	16	0.9	4.8	2.7	1.2	59.12	<i>b</i>	0.04	26
0827+243	21	0.7	6.3	2.5	1.7	98.70	<i>b</i>	0.31	42
0829+046	15	0.9	5.0	2.8	1.5	97.22	<i>b</i>	0.49	<i>c</i>
0836+710	28	1.0	4.5	2.6	1.1	18.05	0.50 [0.31, 0.70]	0.35	25
0851+202	48	0.5	2.1	1.1	0.4	97.90	2.95 [2.82, 3.08]	0.08	17
0954+658	36	0.3	2.1	1.0	0.5	>99.73	0.70 [0.45, 0.95]	0.25	45
1055+018	34	0.4	3.4	1.5	0.8	99.31	0.60 [0.30, 0.90]	0.26	24
1101+384	4	1.3	2.7	2.7	0.6	<i>a</i>	<i>a</i>	<i>a</i>	<i>a</i>
1127-145	20	0.6	3.8	1.9	1.0	63.08	<i>b</i>	0.11	29
1156+295	21	0.9	6.1	2.5	1.5	94.35	<i>b</i>	0.30	30
1219+285	9	0.6	7.4	3.4	2.4	<i>a</i>	<i>a</i>	<i>a</i>	<i>a</i>
1222+216	37	0.4	2.8	1.4	0.7	>99.73	0.60 [0.38, 0.81]	0.37	107
1226+023	32	0.4	5.3	1.3	1.4	88.47	0.80 [0.56, 1.04]	0.56	26
1253-055	32	0.7	2.3	1.2	0.4	35.78	2.95 [2.89, 3.01]	0.15	39
1308+326	25	0.4	6.1	2.6	1.5	95.88	<i>b</i>	0.43	146
1406-076	6	0.5	5.8	3.0	2.0	<i>a</i>	<i>a</i>	<i>a</i>	<i>a</i>
1510-089	21	0.8	5.0	2.2	1.0	93.79	<i>b</i>	0.17	27
1611+343	30	0.7	4.2	2.0	0.9	94.73	2.70 [2.36, 3.05]	0.12	116
1633+382	30	0.5	3.1	1.8	0.6	29.99	2.55 [2.31, 2.79]	0.41	19
1641+399	43	0.4	5.7	1.6	1.4	87.56	2.70 [2.55, 2.84]	0.42	127
1730-130	13	0.4	3.4	1.8	0.9	81.77	<i>b</i>	0.14	82
1749+096	34	0.6	4.2	2.1	1.2	99.56	0.70 [0.59, 0.81]	0.33	116
2200+420	41	0.5	1.7	1.0	0.3	87.22	2.80 [2.75, 2.85]	0.12	33
2223-052	19	0.5	4.0	1.8	1.1	95.48	<i>b</i>	0.15	77
2230+114	22	0.6	2.8	1.4	0.6	45.02	<i>b</i>	0.15	38
2251+158	27	0.5	3.0	1.4	0.8	40.98	2.65 [2.51, 2.79]	0.32	28
min	3	0.3	1.7	1.0	0.3	—	0.50 [0.31, 0.70]	0.04	17
max	48	2.3	7.4	3.9	2.4	—	2.95 [2.82, 3.08]	0.56	146
median	21	0.8	4.2	2.6	1.2	—	0.80 [0.60, 2.55]	0.15	38
std. dev.	12	0.5	1.3	0.7	0.5	—	1.02	0.15	40



**Table 5.** Variability analysis for Polarization Angle ( $\chi$ ). Columns are same as in Table 1. Also shown are the minimum number of days for  $\chi$  to rotate by 180° and 90° (rotate) at 3 and 1.3 mm, respectively.

Source	3 mm													1.3 mm												
	$N_{\text{obs}}$	min ( $^{\circ}$ )	max ( $^{\circ}$ )	diff	$\tilde{\chi}$ ( $^{\circ}$ )	$\sigma_{\chi}$ ( $^{\circ}$ )	Prob.	$\beta$	$F_{\text{var}}$	$F_{\text{var}}^*$	$\Delta(\chi)$ (days)	$\tau_0$ (days)	$\tau_0^*$ (days)	$N_{\text{obs}}$	min ( $^{\circ}$ )	max ( $^{\circ}$ )	diff	$\tilde{\chi}$ ( $^{\circ}$ )	$\sigma_{\chi}$ ( $^{\circ}$ )	Prob.	$\beta$	$F_{\text{var}}$	$\Delta(\chi)$ (days)	$\tau_0$ (days)		
0219+428	30	-106	51	157	-5	27	>99.73	3.00 [2.91, 3.09]	0.29	0.29	$a$ / 170	40	40	4	-42	37	79	34	35	$a$	$a$	$a$	$a$	$a$		
0235+164	50	-238	89	327	-177	92	>99.73	2.75 [2.58, 2.92]	0.64	0.76	244 / 96	793	184	14	-253	-7	246	-168	57	>99.73	$b$	0.81	196 / 15	71		
0316+413	54	-169	59	228	-42	51	>99.73	1.05 [0.84, 1.25]	0.53	0.53	295 / 16	86	85	24	-163	126	289	-10	73	>99.73	$b$	0.55	30 / 21	52		
0336+019	36	29	123	94	76	30	>99.73	1.00 [0.70, 1.32]	0.62	0.63	$a$ / 868	601	106	14	25	113	88	73	28	>99.73	$b$	0.66	$a$	56		
0355+508	76	-49	165	214	88	50	>99.73	2.90 [2.66, 3.14]	0.55	0.32	518 / 98	426	305	34	-24	210	234	119	55	>99.73	1.75 [1.46, 2.06]	0.42	518 / 6	16		
0415+379	87	-276	276	552	-24	161	>99.73	1.40 [1.29, 1.51]	0.57	0.52	109 / 25	$c$	$c$	43	-145	321	466	-4	132	>99.73	1.40 [1.23, 1.56]	0.40	78 / 12	$c$		
0420+014	46	-179	118	297	-37	73	>99.73	2.35 [2.11, 2.59]	0.44	0.45	239 / 52	$c$	$c$	29	-216	51	267	-16	62	>99.73	2.60 [2.36, 2.84]	0.38	81 / 28	164		
0430+052	24	-84	38	122	-20	36	>99.73	$b$	0.40	0.41	$a$ / 19	63	63	12	-220	100	320	29	81	>99.73	$b$	0.40	12 / 12	$c$		
0528+134	66	-221	43	264	-65	63	>99.73	1.65 [1.31, 1.98]	0.38	0.38	145 / 27	130	152	21	-250	28	278	-42	71	>99.73	$b$	0.36	44 / 44	102		
0716+714	108	-116	295	411	147	113	>99.73	2.45 [2.25, 2.65]	0.43	0.31	95 / 29	598	$a$	60	-109	382	491	193	141	>99.73	2.05 [1.86, 2.25]	0.36	37 / 0	743		
0735+178	52	-91	86	177	-49	38	>99.73	0.50 [0.37, 0.63]	0.74	0.73	$a$ / 49	451	186	21	-68	119	187	-9	56	>99.73	$b$	0.83	468 / 168	69		
0827+243	71	-268	106	374	2	97	>99.73	1.40 [1.11, 1.68]	0.52	0.41	232 / 39	$c$	$c$	32	-254	117	371	15	79	>99.73	0.75 [0.62, 0.88]	0.45	148 / 14	394		
0829+046	52	-174	77	251	-81	70	>99.73	2.65 [2.48, 2.82]	0.53	0.46	396 / 140	529	579	16	-145	77	222	-92	58	>99.73	$b$	0.75	566 / 270	79		
0836+710	91	-272	219	491	-108	129	>99.73	1.75 [1.60, 1.90]	0.45	0.47	145 / 30	$c$	$c$	38	-300	111	411	-113	106	>99.73	1.45 [1.12, 1.77]	0.57	144 / 9	20		
0851+202	92	-97	27	124	-32	21	>99.73	1.40 [1.13, 1.67]	0.24	0.23	$a$ / 485	303	62	49	-57	8	65	-33	15	>99.73	3.00 [2.87, 3.13]	0.44	$a$	55		
0954+658	79	-19	65	84	1	18	>99.73	$b$	0.65	0.61	$a$	36	36	36	-28	29	57	-1	14	>99.73	$b$	0.36	$a$	18		
1055+018	60	-101	68	169	-27	36	>99.73	2.05 [1.80, 2.29]	0.34	0.35	$a$ / 132	195	282	38	-123	48	171	-13	38	>99.73	2.85 [2.63, 3.06]	0.26	$a$ / 29	8		
1101+384	25	-78	14	92	-32	26	>99.73	$b$	0.55	0.56	$a$ / 663	45	45	7	-63	35	98	-13	29	$a$	$a$	$a$	$a$ / 138	20		
1127+145	55	-129	8	137	-61	31	>99.73	1.30 [0.96, 1.63]	0.32	0.29	$a$ / 171	417	493	26	-134	113	247	-47	75	>99.73	1.60 [1.25, 1.94]	0.47	278 / 13	20		
1156+295	58	-39	177	216	69	52	>99.73	2.25 [1.97, 2.54]	0.54	0.59	116 / 42	93	101	30	-44	220	264	68	75	>99.73	0.55 [0.41, 0.69]	0.58	33 / 13	0		
1219+285	33	-127	27	154	-84	48	>99.73	0.95 [0.77, 1.13]	0.63	0.64	$a$ / 30	362	280	11	-118	33	151	-69	48	>99.73	$b$	0.80	$a$ / 354	20		
1222+216	60	-22	93	115	-8	28	>99.73	2.50 [2.31, 2.69]	0.74	0.71	$a$ / 61	180	100	37	-46	101	147	-8	22	>99.73	2.70 [2.49, 2.92]	0.53	$a$ / 9	20		
1226+023	82	-74	-14	60	-44	13	>99.73	$b$	0.35	0.32	$a$	51	73	40	-111	36	147	-46	29	>99.73	0.50 [0.26, 0.75]	0.35	$a$ / 15	15		
1253+055	77	-192	220	412	-53	129	>99.73	2.65 [2.47, 2.83]	0.54	0.57	168 / 35	$c$	$c$	34	-118	223	341	5	129	>99.73	3.00 [2.69, 3.32]	0.68	22 / 22	2		
1308+326	54	-183	13	196	-83	46	>99.73	1.25 [1.10, 1.40]	0.32	0.30	1750 / 55	89	74	32	-185	-12	173	-70	49	>99.73	1.80 [1.53, 2.09]	0.36	$a$ / 42	2		
1406+076	32	-42	162	204	116	64	>99.73	$b$	0.57	0.58	616 / 78	345	339	7	-45	144	189	124	54	$a$	$a$	309 / 276	16			
1510+089	53	-277	300	577	-81	129	>99.73	2.25 [2.13, 2.37]	0.53	0.53	101 / 31	$c$	$c$	27	-238	128	366	-70	97	>99.73	2.00 [1.88, 2.11]	0.59	56 / 14	35		
1611+343	68	-138	271	409	-67	114	>99.73	1.75 [1.63, 1.87]	0.48	0.32	507 / 37	$c$	$c$	36	-157	110	267	-80	52	>99.73	1.65 [1.49, 1.81]	0.43	763 / 26	55		
1633+382	75	-311	230	541	40	164	>99.73	1.65 [1.52, 1.78]	0.36	0.41	133 / 26	$c$	$c$	41	-332	181	513	-21	166	>99.73	$b$	0.42	58 / 9	4		
1641+399	80	-3	103	106	66	24	>99.73	1.70 [1.53, 1.86]	0.33	0.33	$a$ / 22	100	54	49	-37	116	153	66	36	>99.73	1.10 [0.97, 1.23]	0.38	$a$ / 2	1		
1730+130	48	-247	72	319	-52	90	>99.73	2.35 [2.06, 2.64]	0.64	0.61	147 / 45	$c$	$c$	18	-132	87	219	14	74	>99.73	$b$	0.44	42 / 42	55		
1749+096	60	-228	82	310	-23	71	>99.73	2.00 [1.85, 2.15]	0.32	0.29	101 / 56	$c$	$c$	42	-171	167	338	-31	91	>99.73	1.85 [1.73, 1.97]	0.46	23 / 6	1		
2200+420	70	-9	62	71	16	12	>99.73	1.35 [1.25, 1.45]	0.39	0.42	$a$	281	112	42	-11	46	57	9	14	>99.73	1.20 [1.01, 1.39]	0.37	$a$	33		
2223+052	59	-2	119	121	86	28	>99.73	2.55 [2.40, 2.70]	0.42	0.31	$a$ / 614	597	130	21	34	154	120	103	32	>99.73	$b$	0.52	$a$ / 75	2		
2230+114	65	-144	291	435	195	111	>99.73	3.00 [2.69, 3.31]	0.33	0.39	62 / 23	$c$	$c$	27	-87	292	379	193	93	>99.73	3.00 [2.92, 3.09]	0.40	229 / 64	3		
2251+158	79	-206	257	463	-52	113	>99.73	2.95 [2.67, 3.21]	0.58	0.45	91 / 19	769	$a$	38	-228	219	447	-84	134	>99.73	3.00 [2.79, 3.20]	0.48	105 / 21	3		
min	24	-311	-14	60	-177	12	–	0.50 [0.37, 0.63]	0.24	0.23	62 / 16	36	36	4	-332	-12	57	-168	14	–	0.50 [0.26, 0.75]	0.26	12 / 0	6		
max	108	29	300	577	195	164	–	3.00 [2.91, 3.09]	0.74	0.76	1750 / 868	793	798	60	34	382	513	193	166	–	3.00 [2.87, 3.13]	0.83	763 / 354	55		
median	60	-129	72	215	-37	73	–	2.05 [1.65, 2.35]	0.53	0.53	147 / 45	281	141	31	-132	119	240	-4	73	–	1.75 [1.45, 2.00]	0.52	81 / 21	2		
std. dev.	20	80	87	152	97	43	–	0.68	0.12	0.14	368 / 209	241	213	13	85	95	128	89	35	–	0.78	0.17	208 / 89	33		

No rotation > 180°.

**Table 6.** Variability analysis for the rotation measure  $RM$ . Columns are same as six first columns in Table 1

Source	$N_{\text{obs}}$	min [ $\times 10^3 \text{ rad/m}^2$ ]	max [ $\times 10^3 \text{ rad/m}^2$ ]	$\bar{RM}$ [ $\times 10^3 \text{ rad/m}^2$ ]	$\sigma_{RM}$ [ $\times 10^3 \text{ rad/m}^2$ ]
0219+428	4	-32	49	-14	32
0235+164	14	-225	57	-45	101
0316+413	21	-190	80	-31	71
0336-019	14	-93	102	-4	60
0355+508	34	-179	114	-21	63
0415+379	41	-218	91	-6	75
0420-014	29	-122	73	15	47
0430+052	11	-166	63	-73	91
0528+134	21	-156	106	7	78
0716+714	60	-219	119	-6	83
0735+178	21	-157	36	-56	63
0827+243	32	-160	123	17	76
0829+046	16	-101	27	-16	31
0836+710	38	-172	122	13	75
0851+202	49	-108	19	-4	23
0954+658	36	-51	52	-2	22
1055+018	38	-138	77	-7	51
1101+384	7	-134	113	-17	71
1127-145	25	-205	107	1.1	91
1156+295	29	-181	97	-40	72
1219+285	11	-155	82	-13	58
1222+216	37	-47	114	-6	33
1226+023	40	-161	85	11	49
1253-055	34	-182	56	7	68
1308+326	32	-103	74	-12	44
1406-076	7	-51	35	-2	33
1510-089	27	-138	87	-3	57
1611+343	36	-132	131	20	61
1633+382	41	-191	88	7	77
1641+399	49	-65	120	1.3	44
1730-130	18	-142	36	9	50
1749+096	41	-221	136	13	81
2200+420	42	-12	29	6	10
2223-052	21	-75	111	-3	53
2230+114	27	-168	116	-15	56
2251+158	38	-158	64	-2	52
min	4	-225	19	-73	10
max	60	-12	136	20	101
median	30	-166	74	-12	68
std. dev.	13	52	29	26	19

## APPENDIX A: ANALYSIS TOOLS

The statistical methods and definitions used in this paper as analysis tools for the interpretation of our data are presented in this Appendix. These include:

(i)  *$\chi^2$  test for variability.* We tested the variability of the data from the  $\chi^2$  obtained from fitting a constant against the distributions built from our time-dependent data sets. The resulting probability along with the  $\chi^2$  and the degrees of freedom for every analysed variable are given in the Tables shown in this paper (e.g. Table 1 for the analysis of total flux results).

(ii) *Power spectral density.* We estimated the power spectral density (PSD) slopes under the assumption that the underlying model resembles a power-law ( $\text{PSD} \propto f^{-\beta}$ ). A variant of the Power Spectral Response method (Uttley et al. 2002) as detailed in Ramakrishnan et al. (2015) was used for estimating the slopes. This method involves the comparison of the observed periodogram against those obtained using the simulated time-dependent data sets. The data trains were simulated following the method proposed by Emmanoulopoulos et al. (2013), which accounts for the PSD slope and the distribution of the data. To circumvent the problems imposed by the finite length and uneven sampling of the observed data on the estimation of the PSD slope, we simulated data trains with increased time resolution and 100 times longer than the observed ones, and through the convolution of Hanning window function with the observed data following Max-Moerbeck et al. (2014). We also added Gaussian noise with variance matching those of the observations for the simulated data before resampling the simulated light curves. We ran this simulation for the PSD slopes in the range, 0.5–3, in steps of 0.05. The probability at every slope was obtained from a goodness of fit statistic that compares the average and standard deviation of the simulated periodograms with those of the observed ones. The best-fit PSD slope was taken as the one with the highest probability. PSD slopes were estimated only for those cases where more than 10 actual measurements were available in a data train.

(iii) *Fractional variability amplitude.* To quantify the relative amount of variability of every variable measured on every source we estimated the fractional root mean squared variability amplitude (or fractional variability amplitude,  $F$ ) from the relation (Vaughan et al. 2003):

$$F = \sqrt{\frac{S^2 - \sigma_{\text{err}}^2}{\bar{x}^2}}, \quad (\text{A1})$$

where  $S^2$ ,  $\sigma_{\text{err}}^2$  and  $\bar{x}^2$  are the variance, the mean squared error, and the squared arithmetic mean of every data train, respectively. The uncertainty on  $F$ , was computed and discussed by Vaughan et al. (2003), and is expressed as:

$$\text{err}(F) = \sqrt{\left\{ \sqrt{\frac{1}{2N} \frac{\sigma_{\text{err}}^2}{\bar{x}^2 F}} \right\}^2 + \left\{ \sqrt{\frac{\sigma_{\text{err}}^2}{N}} \frac{1}{\bar{x}} \right\}^2}, \quad (\text{A2})$$

where  $N$  is the number of points in every data train.

(iv) *Correlation analysis.* The correlated variability between different variables were studied using the discrete correlation function (DCF) of Edelson & Krolik (1988). This method is efficient when the sampling of the observed data is uneven. The DCF is defined as:

$$\text{DCF}_{ij} = \frac{(a_i - \bar{a})(b_j - \bar{b})}{\sigma_a \sigma_b}, \quad (\text{A3})$$

where  $a_i, b_j$  are the observed data at times  $t_i$  and  $t_j$  and  $\bar{a}, \bar{b}, \sigma_a$  and  $\sigma_b$  are the means and standard deviations of the entire data trains of variables  $a$  and  $b$ , respectively.

Unlike most other work that bin the data using equal widths, here we bin the associated time-lag such that it mitigates the chances of overlapping with the adjacent bins. This condition is ensured by the resolution parameter ( $\epsilon$ ), that is defined such that  $\tau_{i+1} - \tau_i < \epsilon$ . In this process, we also ensure that there are at least 10 points within each bin, see Alexander (2013) for more details on the binning method used here.

The average of the bins yields the  $\text{DCF}(\tau)$ . Following Welsh (1999), we applied the local normalisation to the DCF, which restricts the peak within  $[-1, +1]$  interval. The uncertainties on the DCF were estimated from a model-independent Monte Carlo method (Peterson et al. 1998).

We tested the significance of the DCF peak by cross-correlating 5000 data trains simulated using the best-fit PSD slopes. Based on this simulation, at every time-lag we constructed a cross-correlation distribution from which the 99.73 % significance levels were determined.

Using the DCF relation shown in equation A3 and the procedure employed to estimate the cross-correlation, we also computed the autocorrelation functions (ACF) of every variable analysed in this work. The zero-crossing time of the main lobe of the ACF ( $\tau_0$ ) provides an estimate of the time scale of variability, that we show for every variable and every source in the tables presented in this work.

For all methods and definitions discussed above, only those measurements with modulus larger than the measurement uncertainty were considered, except for the case of the variability study of the linear polarisation angle.

This paper has been typeset from a  $\text{T}_{\text{E}}\text{X}/\text{L}^{\text{A}}\text{T}_{\text{E}}\text{X}$  file prepared by the author.

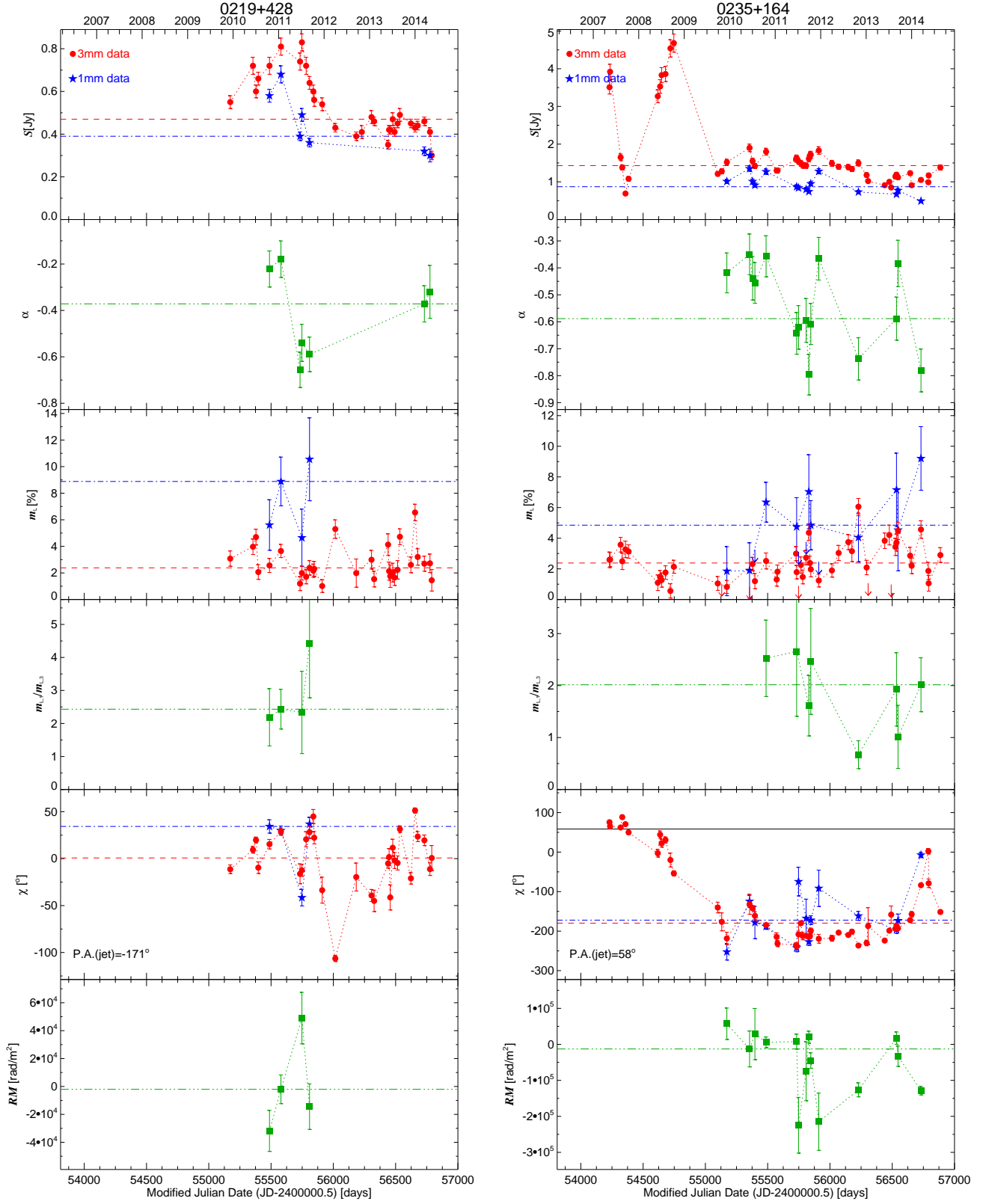


**Figure 11.** Daily averages of 3 mm (red circles) and 1 mm (blue stars) fully calibrated measurements of total flux ( $S$ ), linear polarisation degree ( $m_L$ ), and polarisation angle ( $\chi$ ) of the 36 sources in the POLAMI sample of variable sources as a function of time. Comparison of these quantities at the two wavelengths are also shown (by green squares) for the spectral index ( $\alpha$ ), ratio of 1 mm to 3 mm polarisation degree ( $m_{L,1}/m_{L,3}$ ), and rotation measure ( $RM$ ). Arrows are  $2\sigma$  upper limits. The red dashed and blue dash-dotted lines indicate medians of 3 and 1 mm values on every one of the plots, respectively, whereas dash-dotted-dotted lines represent medians of  $\alpha$ ,  $m_{L,1}/m_{L,3}$ , and  $RM$ . The black continuous line on the  $\chi$  plots symbolises the jet position angle, i.e. P.A. (jet), according to [Jorstad et al. \(2017, ApJ in press\)](#); [Molina et al. \(2014\)](#), see text, but is only plotted for sources for which the values where  $\chi$  ranges include the P.A. (jet) value.



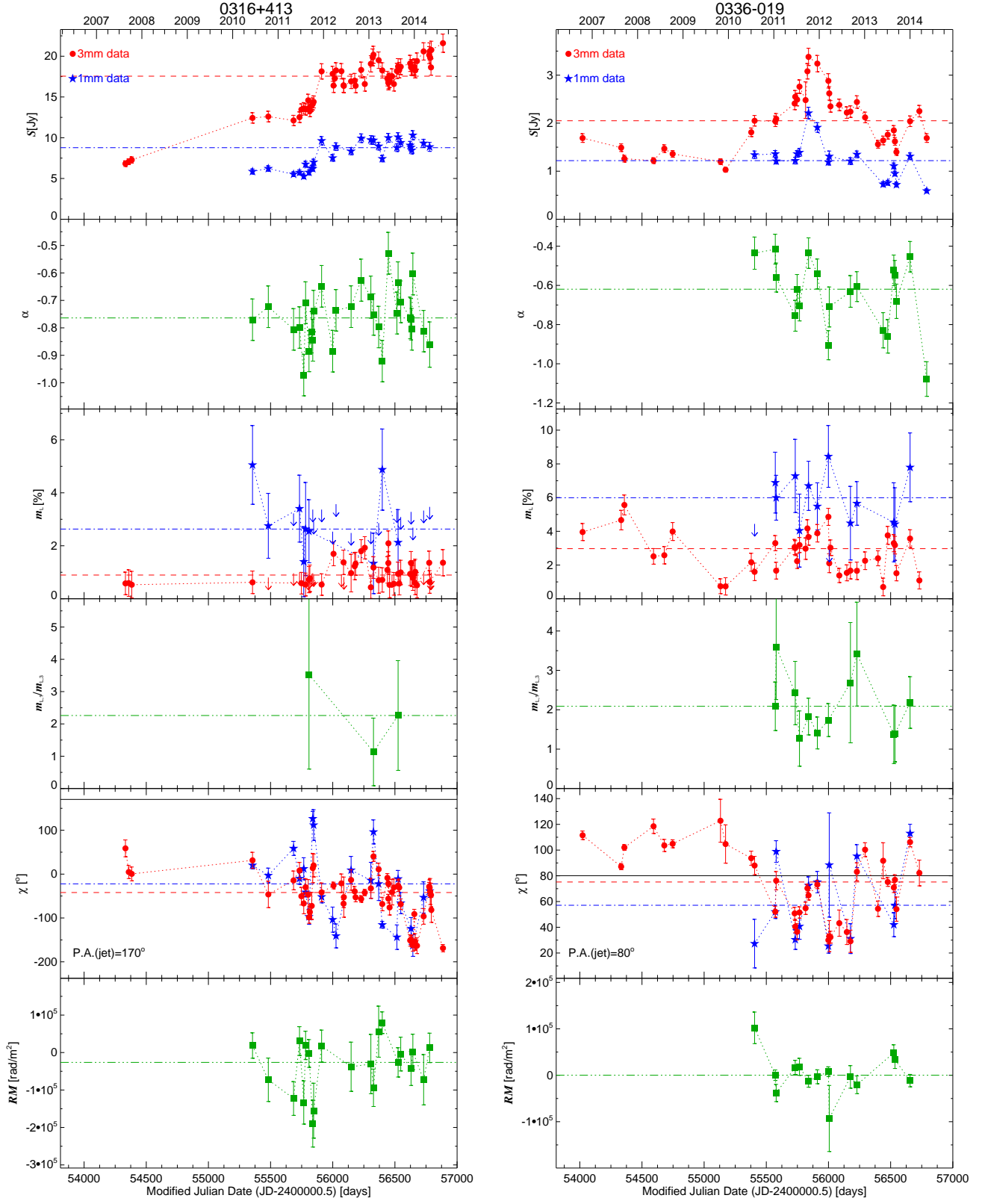


Figure 10. Continued.

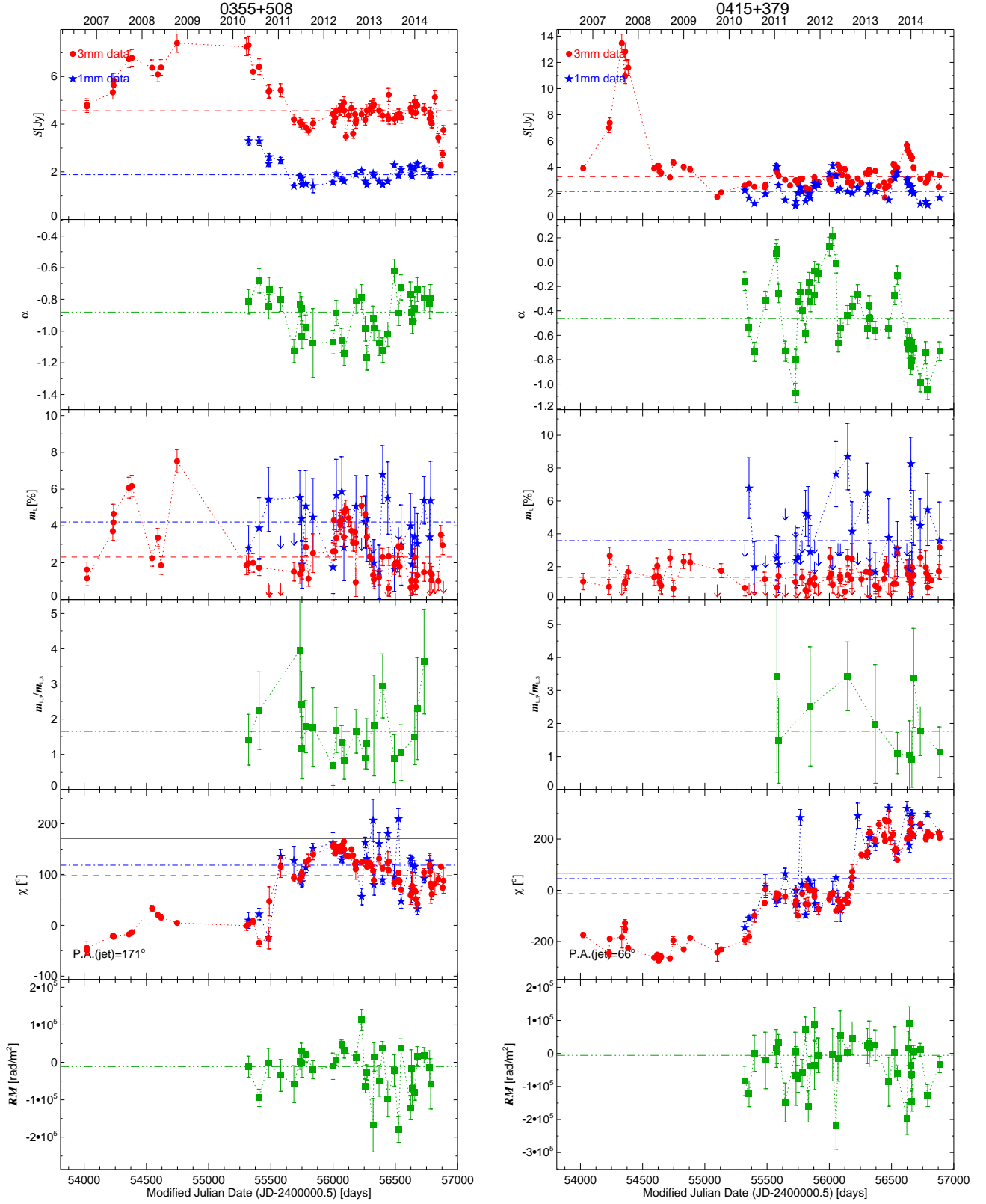


Figure 10. Continued.

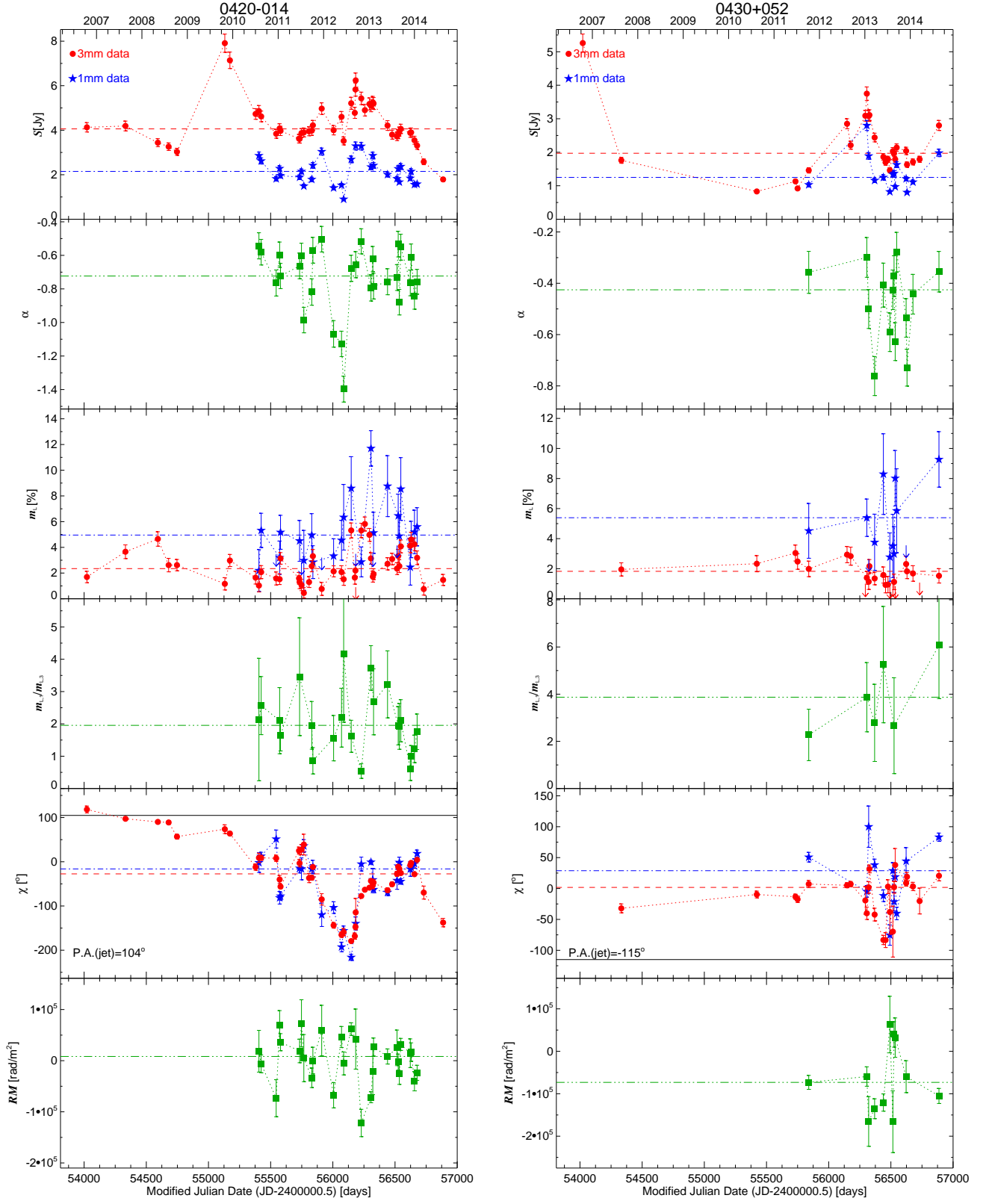


Figure 10. Continued.

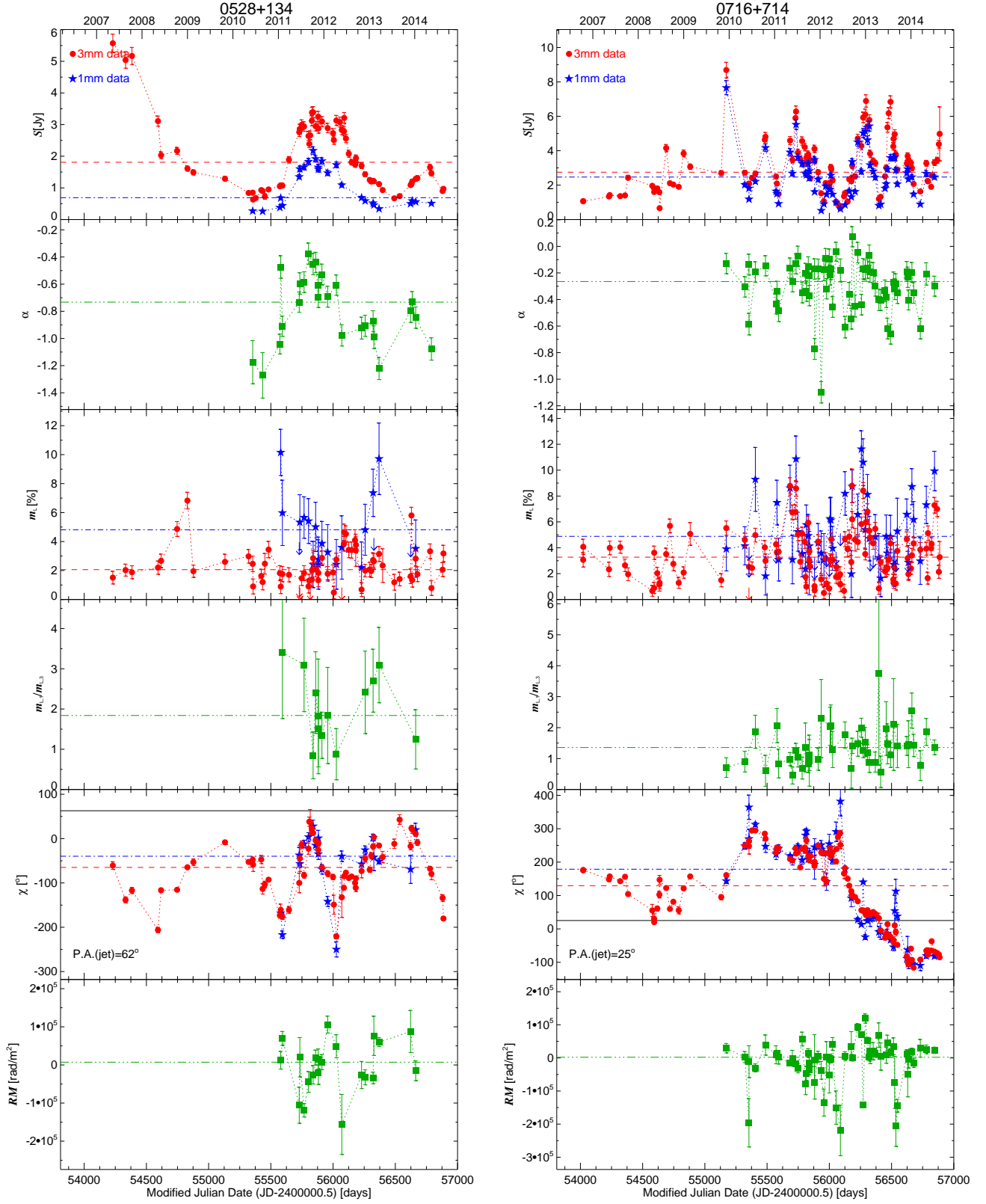


Figure 10. Continued.

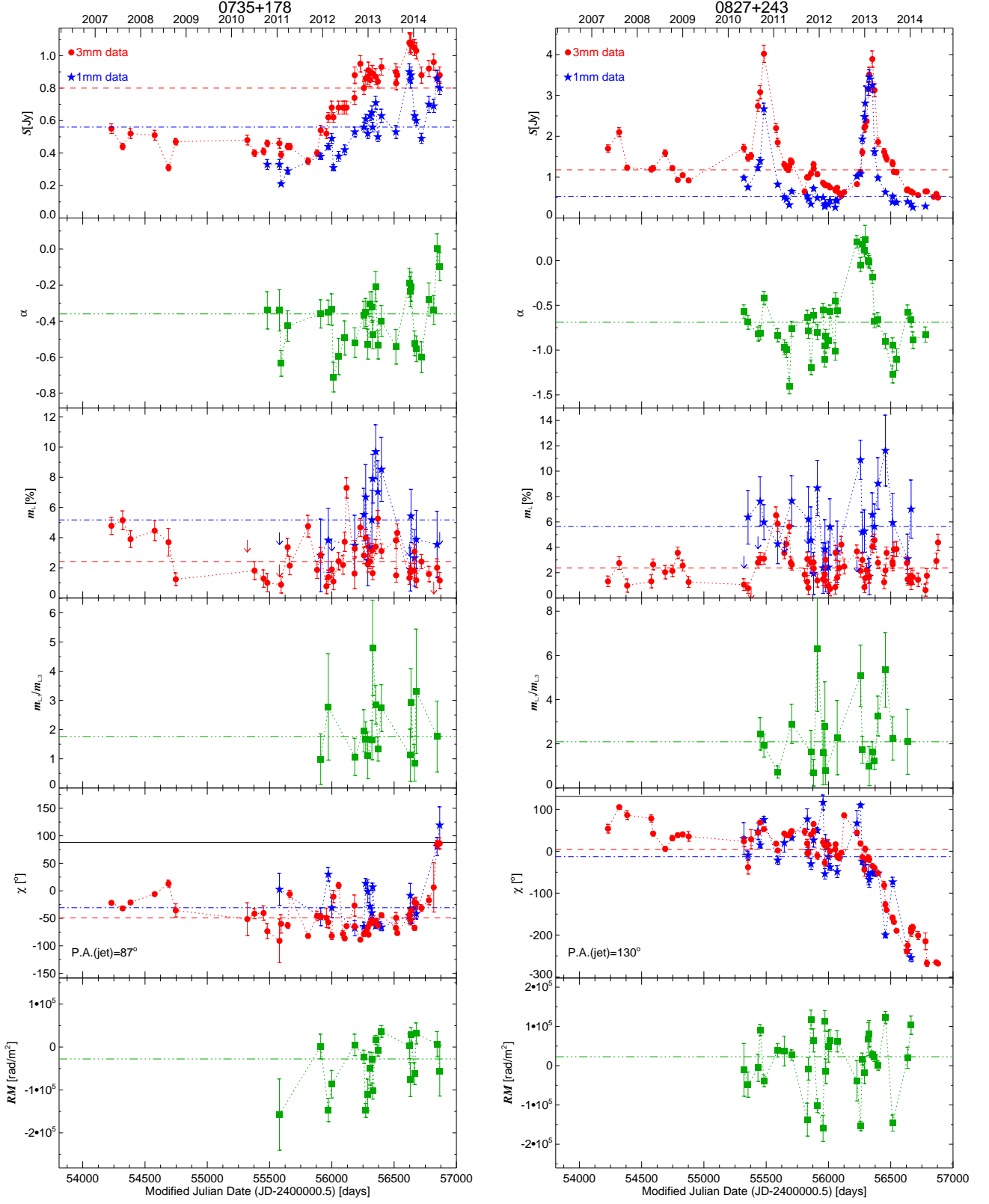


Figure 10. Continued.



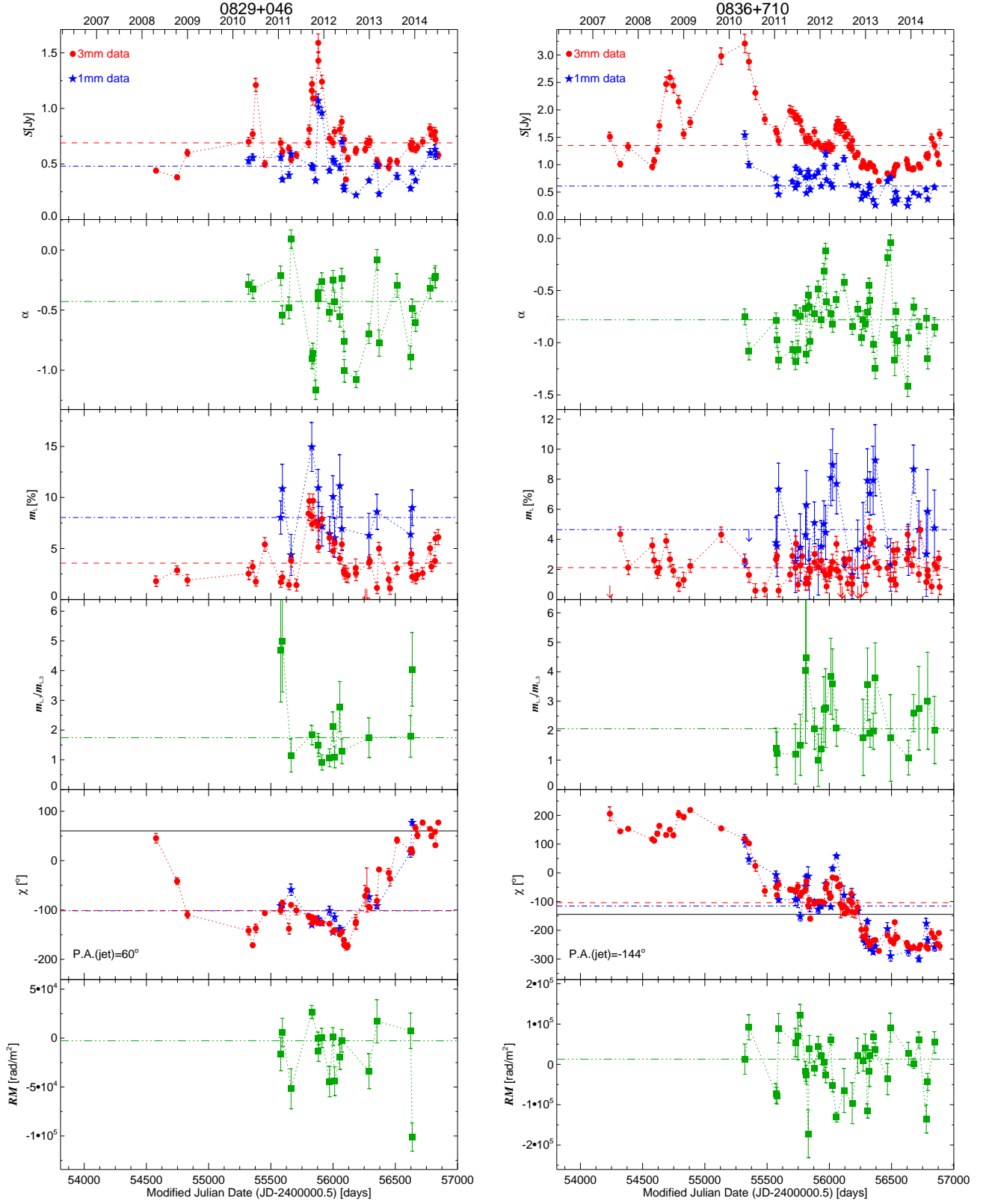


Figure 10. Continued.

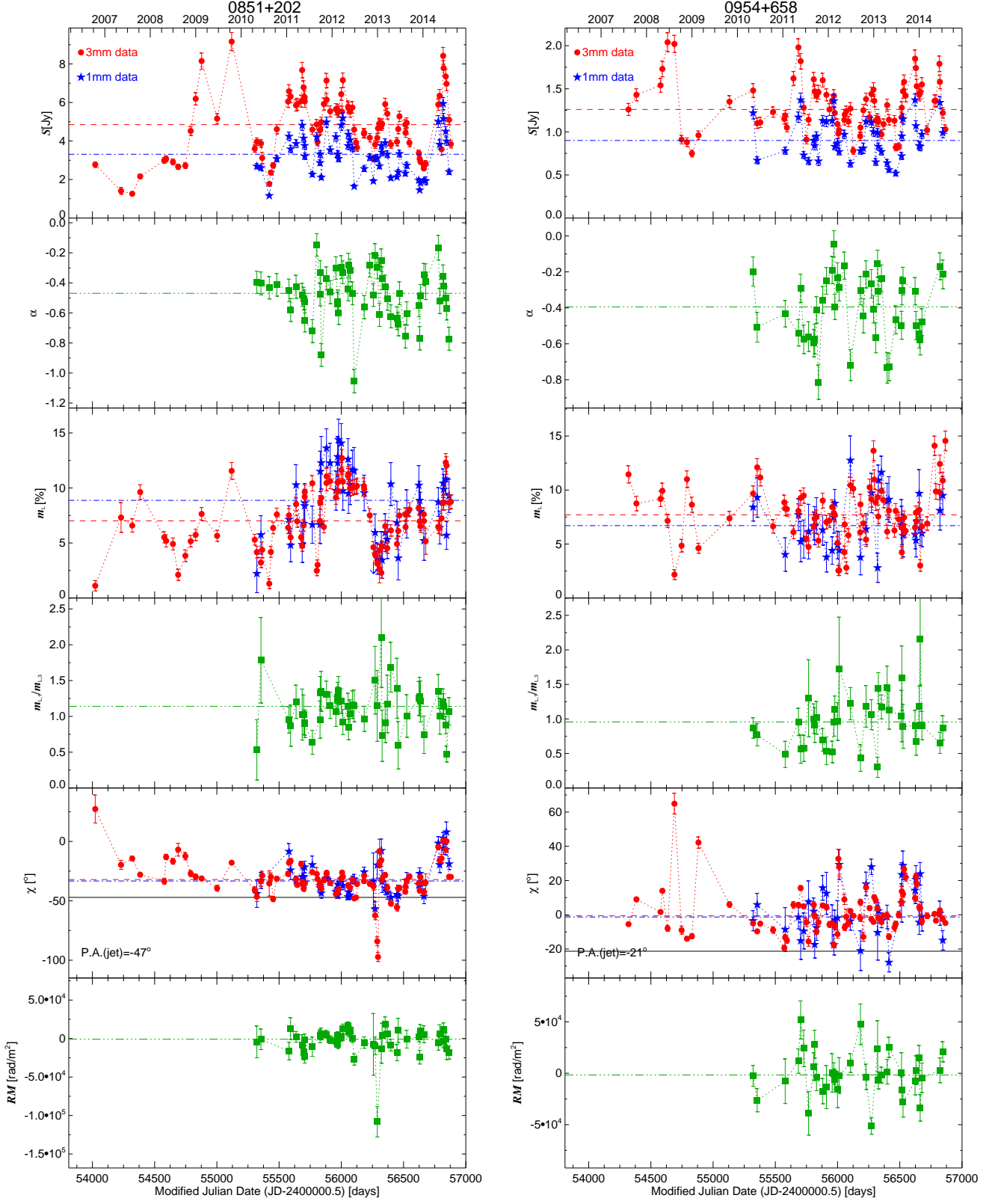


Figure 10. Continued.

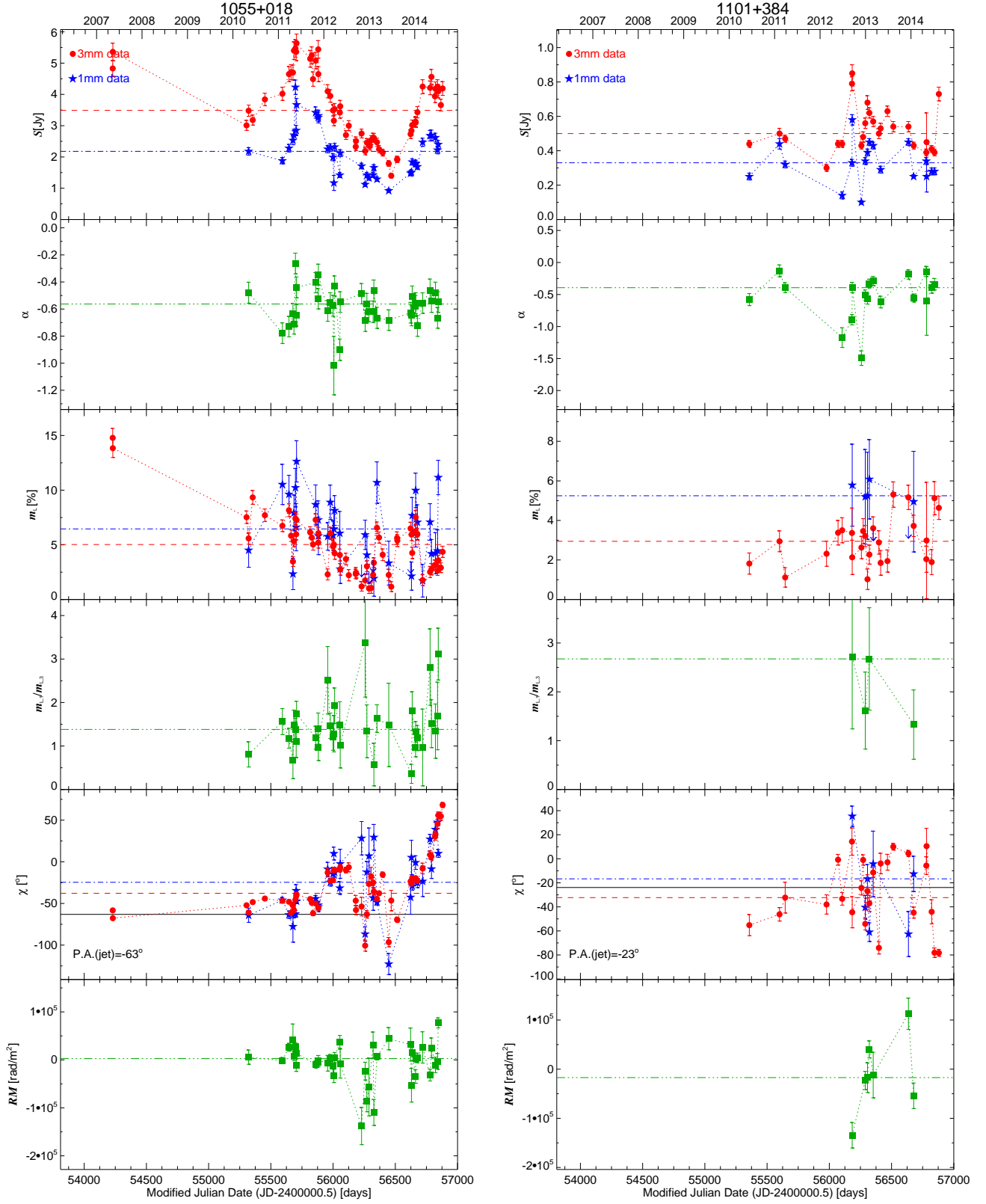


Figure 10. Continued.

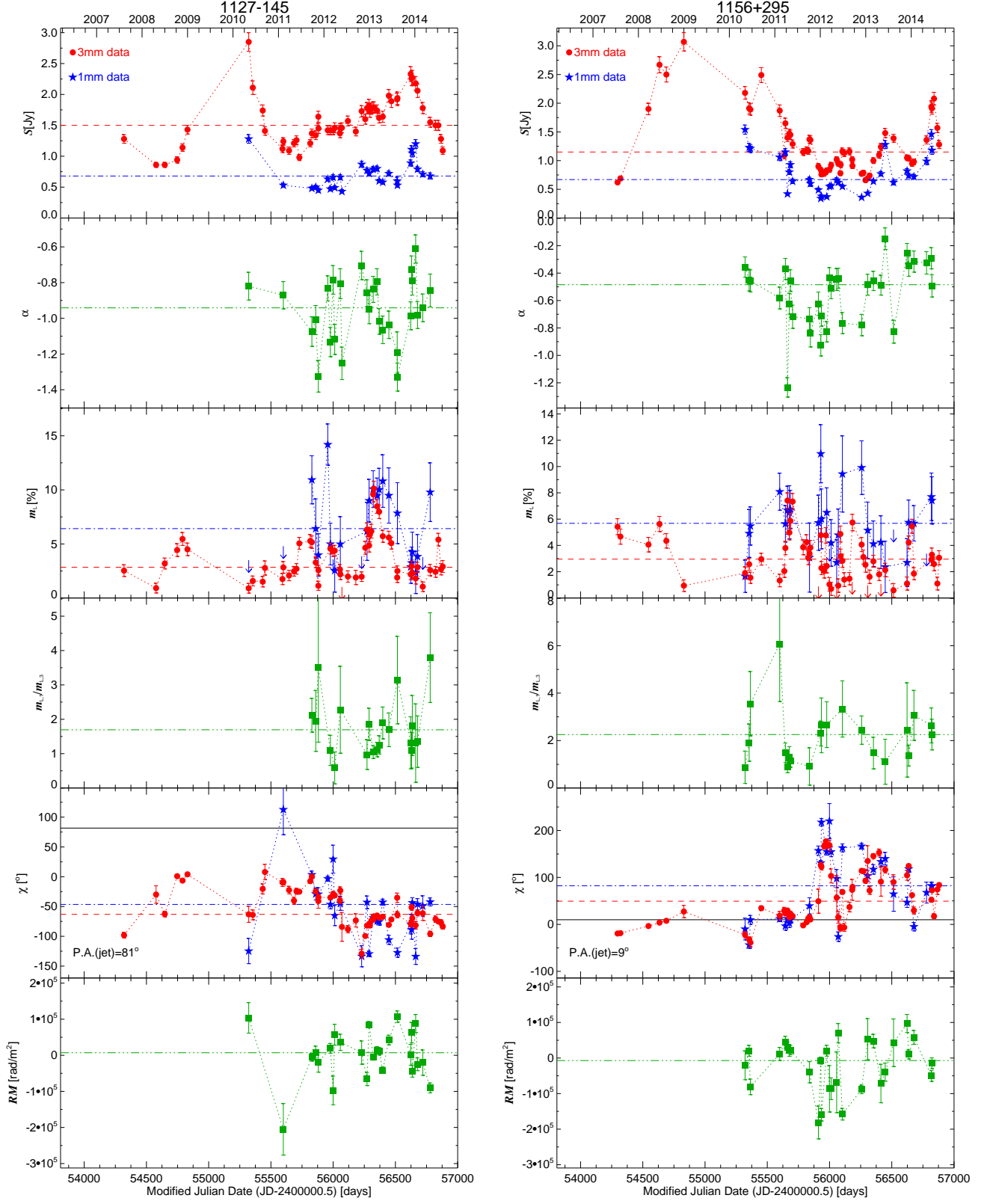


Figure 10. Continued.

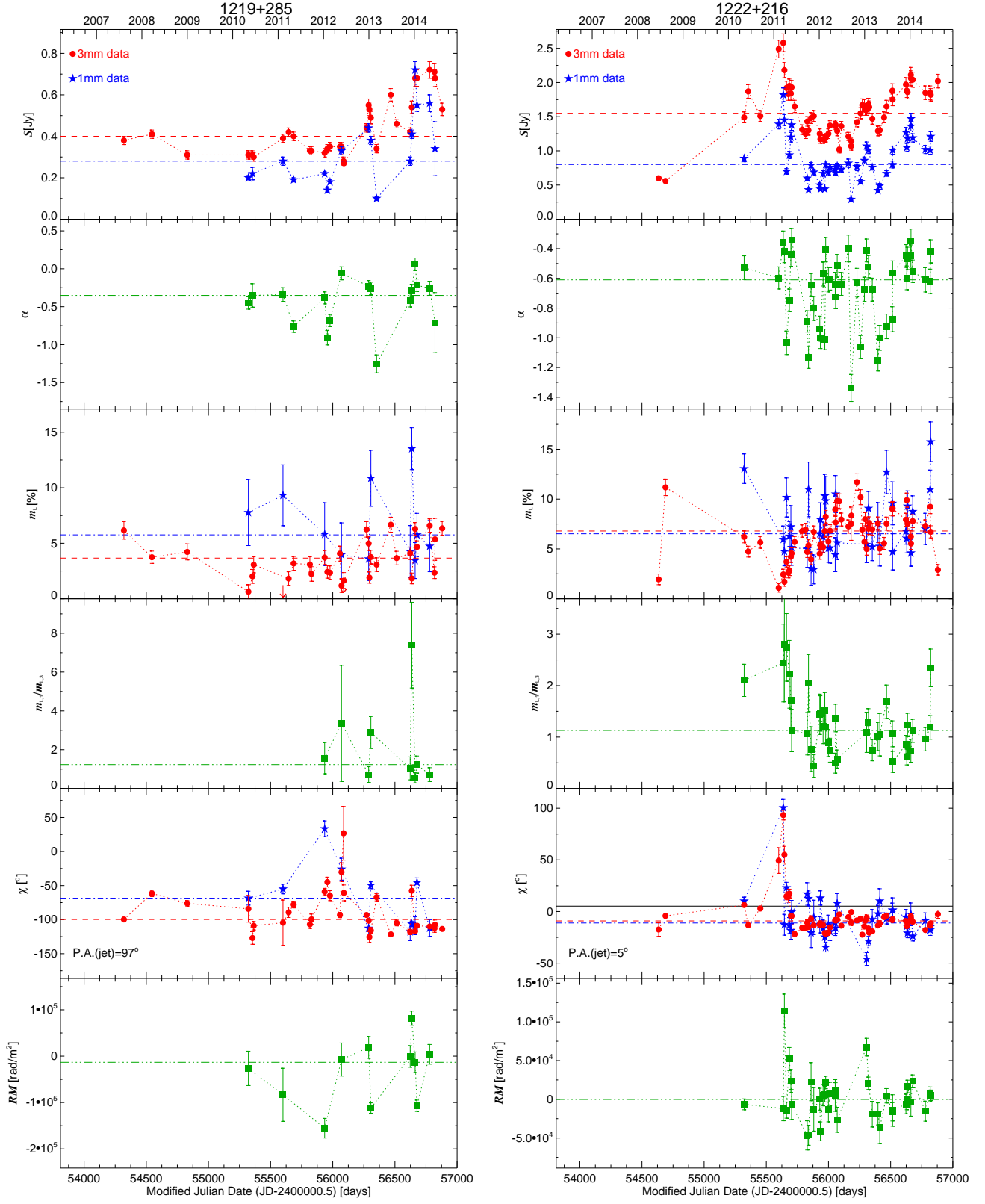


Figure 10. Continued.



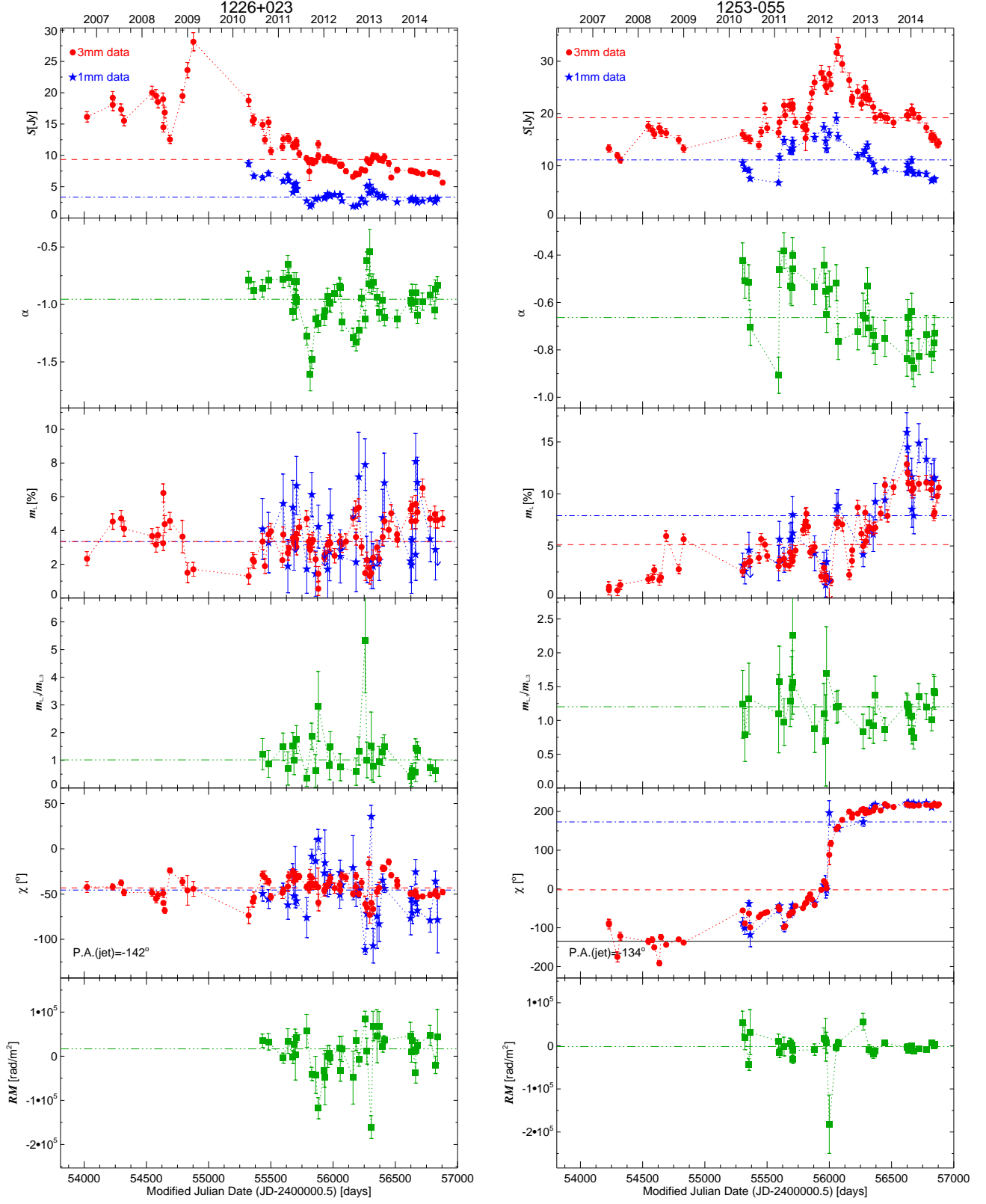


Figure 10. Continued.

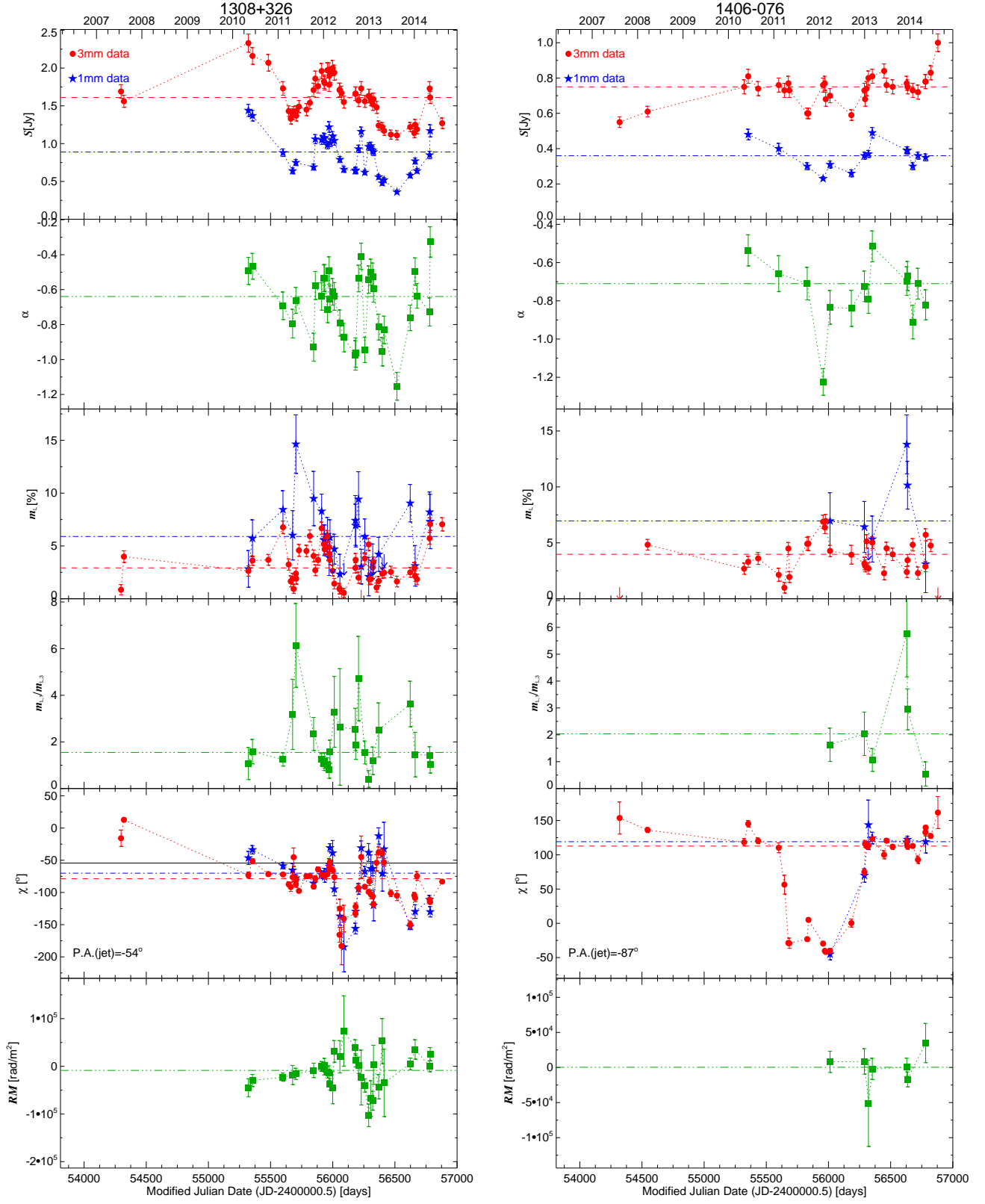


Figure 10. Continued.

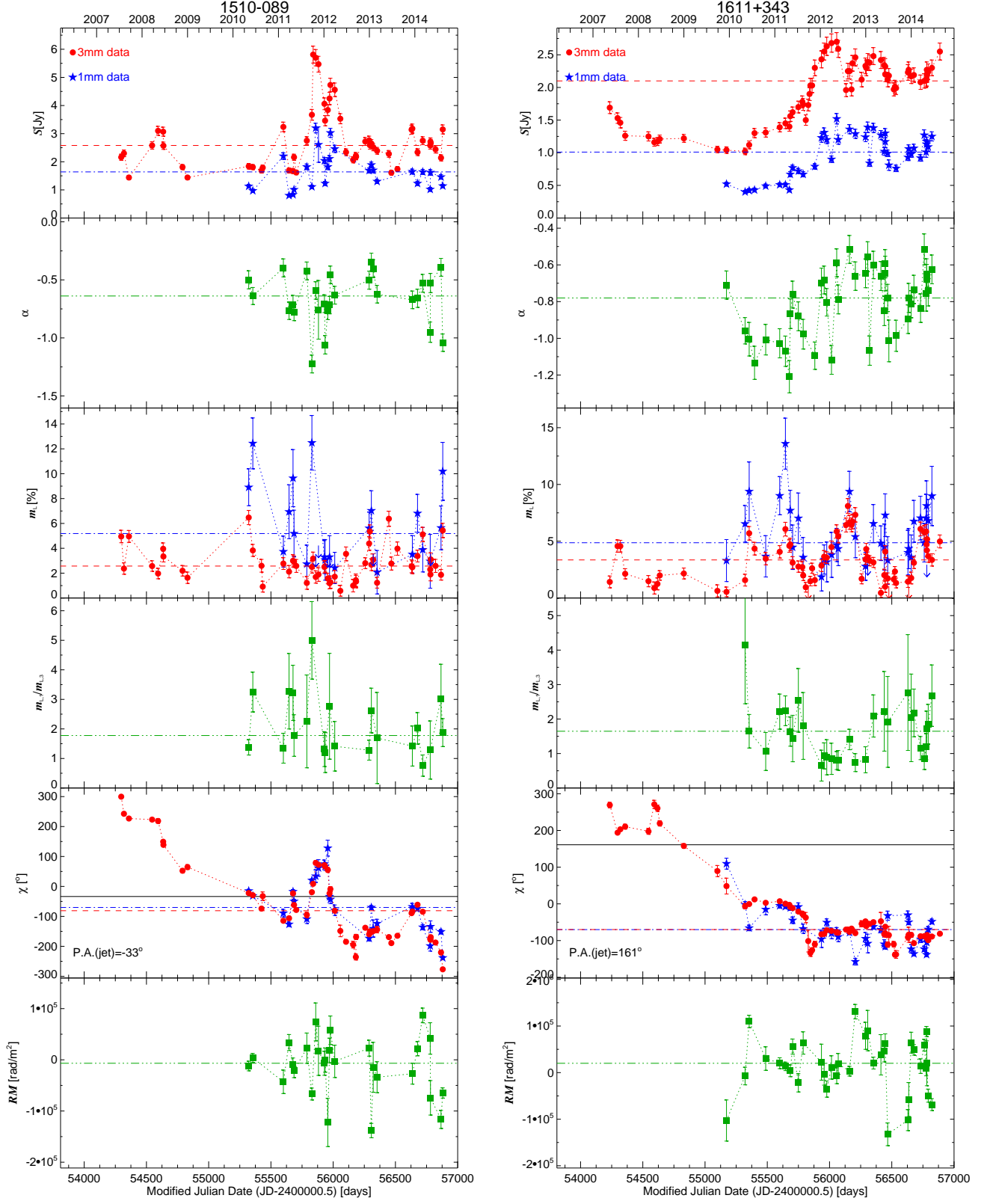


Figure 10. Continued.

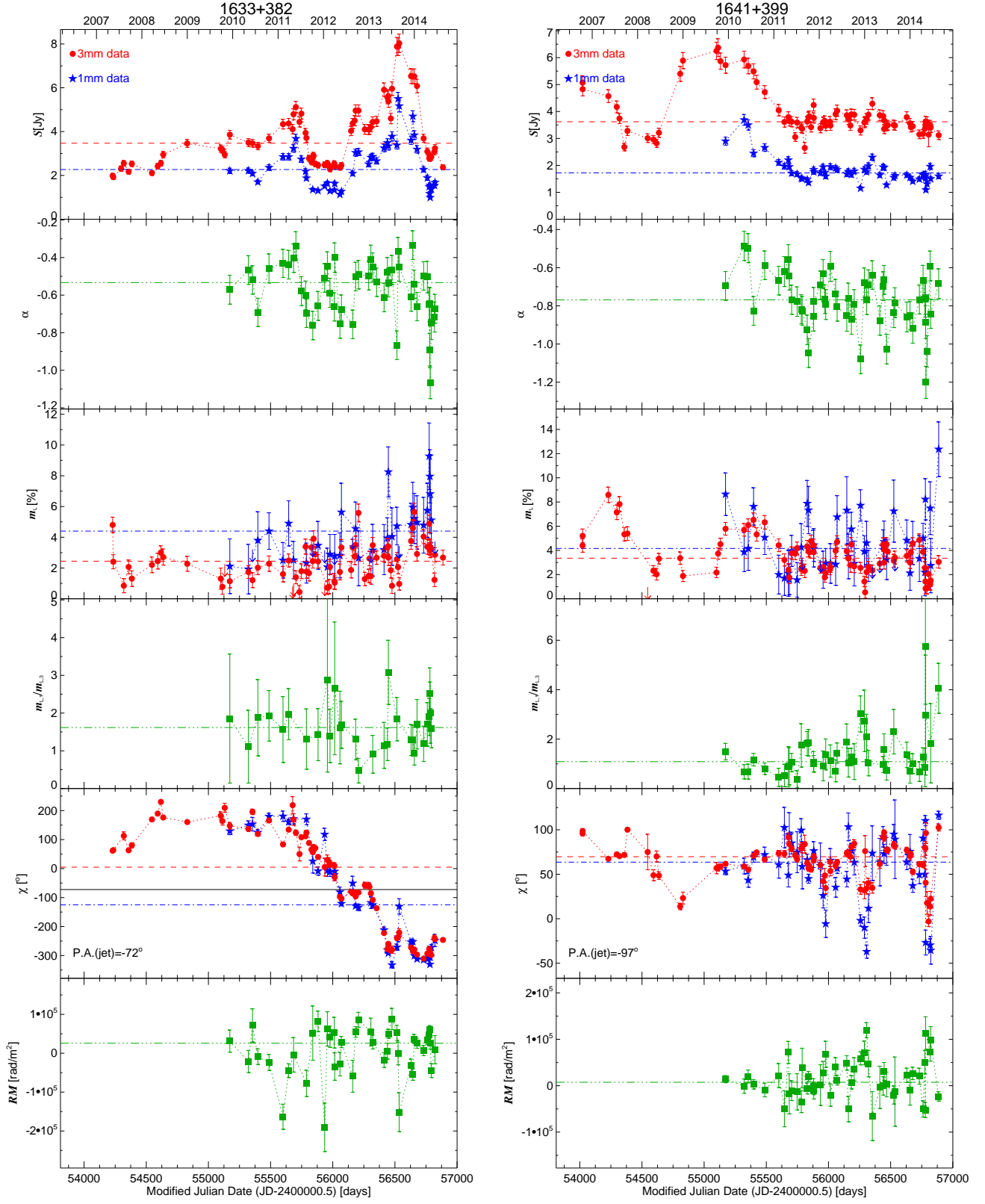


Figure 10. Continued.

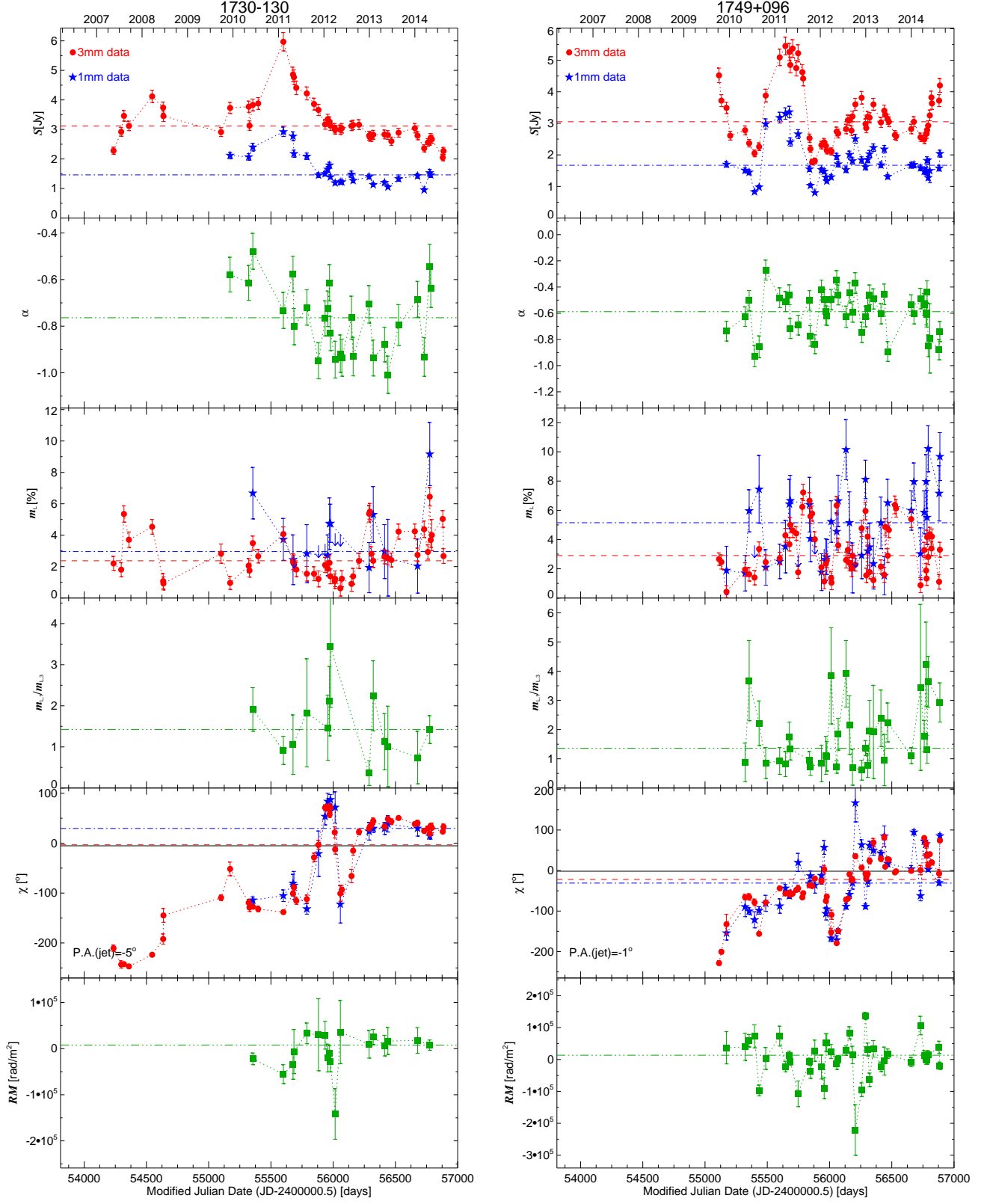


Figure 10. Continued.



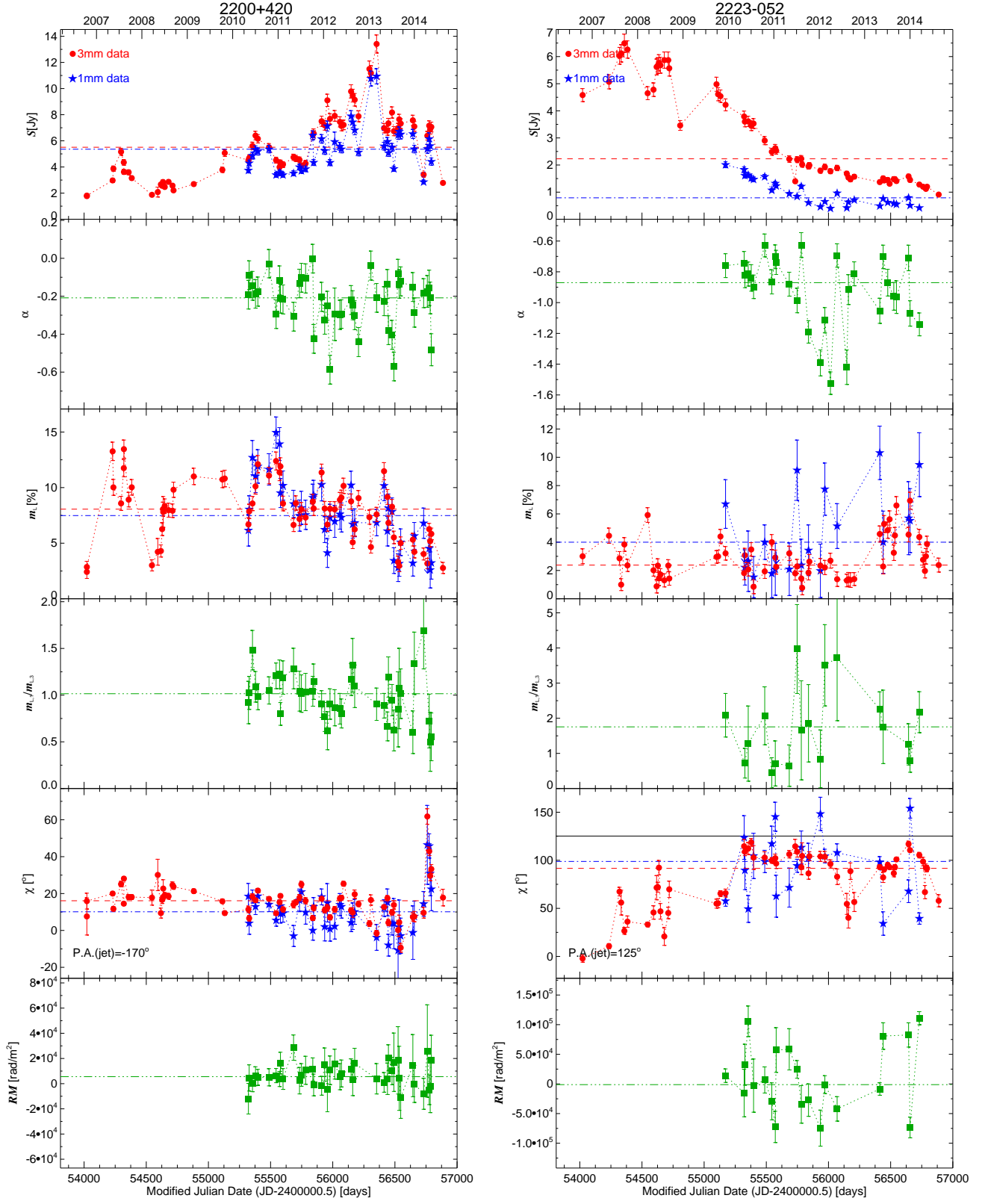


Figure 10. Continued.

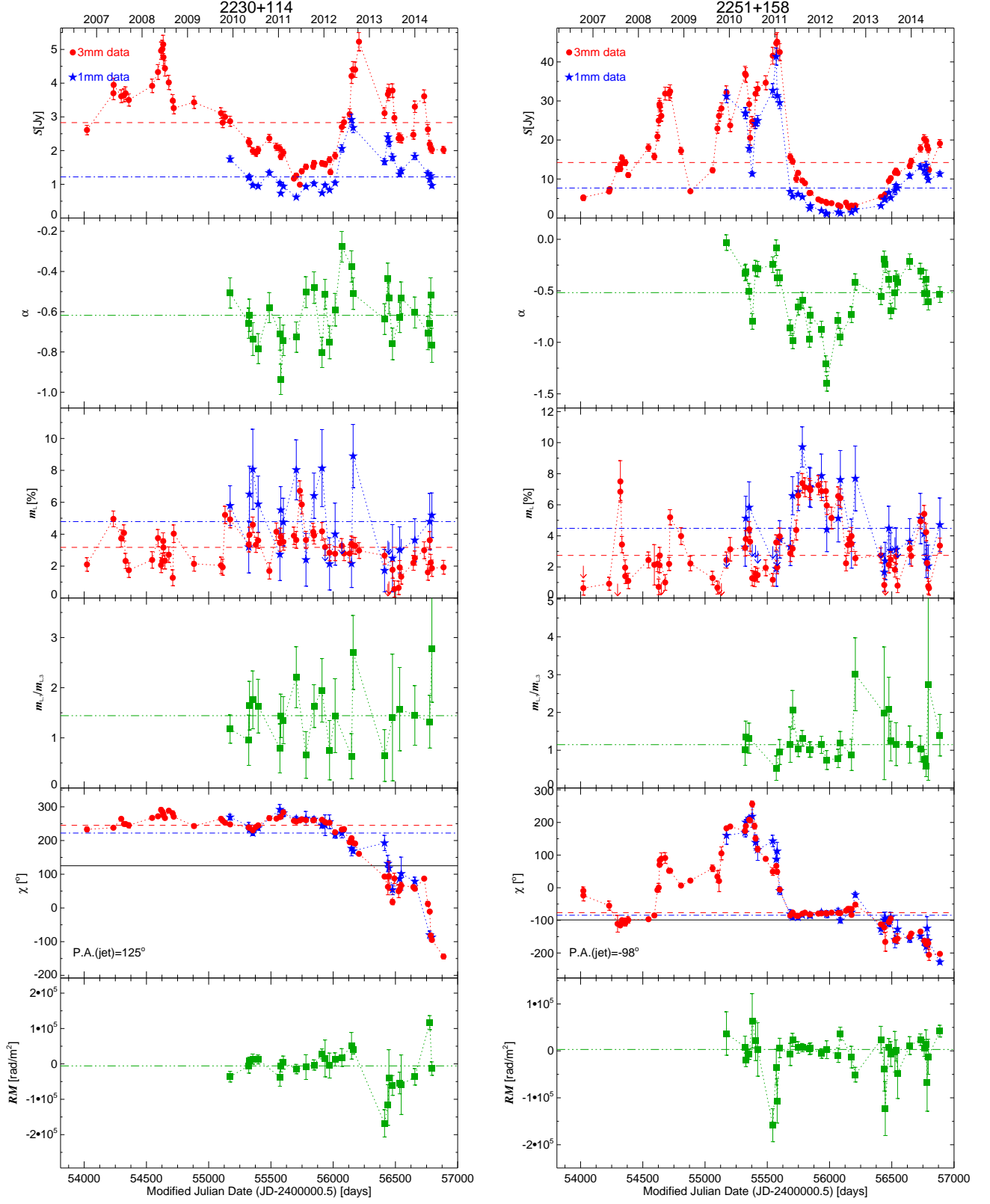


Figure 10. Continued.